Intrinsic macroscale oscillatory modes driving long range functional connectivity detected with ultrafast fMRI

Joana Cabral[1,2†], Francisca F. Fernandes[2], Noam Shemesh[2†]

[1] Life and Health Sciences Research Institute, School of Medicine, University of Minho, Braga, Portugal

[2] Preclinical MRI Lab, Champalimaud Research, Champalimaud Foundation, Lisbon, Portugal

One Sentence Summary: (max 125 char)

Oscillations in fMRI signals organize in stationary wave patterns driving condition-specific long-range correlations across brain structures

[†]Correspondence:

Dr. Noam Shemesh
Preclinical MRI Lab, Champalimaud Research, Champalimaud Foundation
Av. Brasilia 1400-038, Lisbon, Portugal.
E-mail: noam.shemesh@neuro.fchampalimaud.org
Phone number: +351 210 480 000 ext. #4467.

Dr. Joana Cabral
Life and Health Sciences Research Institute, School of Medicine, University of Minho
Campus de Gualtar, 4710-057 Braga, Portugal
E-mail: joanacabral@med.uminho.pt
Phone number: +351 919 289 649

Abstract

Spontaneous fluctuations in functional Magnetic Resonance Imaging (fMRI) signals correlate across distant brain areas, shaping functionally relevant intrinsic networks. However, the generative mechanism of fMRI signal correlations - and in particular their link with locally-detected ultra-slow oscillations - remain unclear. To investigate this link, we record ultrafast ultrahigh field fMRI signals (9.4 Tesla, temporal resolution = 38 milliseconds) from rat brains across three anesthesia conditions. Power at frequencies extending up to 0.3 Hz is detected consistently across rat brains, and is modulated by anesthesia level. Principal component analysis reveals a repertoire of modes, in which transient oscillations organize with fixed phase relationships across distinct cortical and subcortical structures. Oscillatory modes are found to vary between conditions, resonating at faster frequencies under medetomidine sedation and reducing both in number, frequency, and duration with the addition of isoflurane. Peaking in power within clear anatomical boundaries, these oscillatory modes point to an emergent systemic property, questioning current assumptions regarding the local origin of oscillations detected in fMRI and providing novel insights into the organizing principles underpinning spontaneous long-range functional connectivity.

Introduction

Spontaneous fluctuations in signals detected with functional Magnetic Resonance Imaging (fMRI) correlate across spatially distributed brain areas forming functional networks that appear disrupted in numerous psychiatric and neurological disorders, pointing to a key role in brain function (Fox and Raichle 2007, Biswal, Mennes et al. 2010, Stam 2014, Fornito, Zalesky et al. 2015, Gozzi and Zerbi 2022). However, the organizing principle driving long range correlations between brain areas remains unclear.

A wide range of low-rank decomposition techniques have been put forward to characterize the spatial organization of spontaneous fMRI signal fluctuations, including among others independent component analysis (Damoiseaux, Rombouts et al. 2006, Smith, Fox et al. 2009), co-activation patterns (Eickhoff, Bzdok et al. 2011, Liu and Duyn 2013, Liu, Zhang et al. 2018, Gutierrez-Barragan, Basson et al. 2019), low-dimensional gradients (Margulies, Ghosh et al. 2016, Huntenburg, Bazin et al. 2018), leading eigenvector dynamics analysis (Cabral, Vidaurre et al. 2017, Lord, Expert et al. 2019), dynamic mode decomposition (Casorso, Kong et al. 2019) and quasi-periodic patterns (QPPs) (Yousefi, Shin et al. 2018, Bolt, Nomi et al. 2022). Despite the differences inherent to each technique, most methods converge in a discrete repertoire of intrinsic modes exhibiting features of stationary wave patterns, where correlated activity is detected among spatially distributed regions (or poles), with gradually varying phase relationships across space (Uddin, Yeo et al. 2019). These intrinsic modes have been shown to emerge transiently and recurrently during rest (Calhoun, Miller et al. 2014, Preti, Bolton et al. 2017), to be selectively recruited during specific tasks (Smith, Fox et al. 2009) and to replicate across mammals (Hutchison, Leung et al. 2011, Lu, Zou et al. 2012, Fulcher, Murray et al. 2019, Gutierrez-Barragan, Basson et al. 2019, Coletta, Pagani et al. 2020).

In the frequency domain, correlated fluctuations in fMRI signals exhibit power at ultra-slow frequencies, peaking typically below 0.1 Hz in human brains at rest, although intrinsic functional networks have been detected at frequencies extending even beyond 0.5 Hz (Lee, Zahneisen et al. 2013, Chen and Glover 2015, Lewis, Setsompop et al. 2016, Trapp, Vakamudi et al. 2018, Vohryzek, Deco et al. 2020). Crucially, it remains unclear whether the spectral power at low frequencies is associated solely with aperiodic activations of the characteristically slow and region-specific hemodynamic response function or additionally reflects the existence of damped oscillatory components (Gonzalez-Castillo, Saad et al. 2012, Lewis, Setsompop et al. 2016, Cabral, Kringelbach et al. 2017, Casorso, Kong et al. 2019). Mainly detected with electro- and magnetoencephalography (EEG/MEG), macroscale oscillatory components in brain activity have been targeted by neural field theories, demonstrating how the frequency spectrum and correlation structure can be predicted from brain geometry (Mukta, MacLaurin et al. 2017, Gabay, Babaie-Janvier et al. 2018, Tewarie, Abeysuriya et al. 2018). Although intrinsic modes detected with fMRI have been shown to spatially align with eigenmodes of brain structure (either from surface geometry of diffusion networks), theoretical predictions of mode-specific temporal responses remain to be adequately addressed in fMRI (Friston, Kahan et al. 2014, Atasoy, Donnelly et al. 2016, Robinson, Zhao et al. 2016, Xie, Cai et al. 2021). Given recent insights demonstrating that the fMRI signals underpinning intrinsic networks relate to macroscopic waves of propagating activity (Schwalm, Schmid et al. 2017, Casorso, Kong et al. 2019, Gu, Sainburg et al. 2021, Raut, Snyder et al. 2021), it is crucial to obtain a detailed characterization of the modes' spatial and temporal signatures to empirically investigate their oscillatory nature and their link with neural field theories.

Studies in rodents and humans have shown that some ultra-slow frequency components in fMRI signals have a periodic nature and are coupled with electrophysiological

and electroencephalographic (EEG) signals (He, Snyder et al. 2008, Pan, Thompson et al. 2013, Thompson, Pan et al. 2014, Fultz, Bonmassar et al. 2019). These periodic fluctuations have been proposed to be linked to arteriole vibrations entrained by fast oscillations in local field potentials, pointing to a potentially more direct relationship with the underlying neural activity (Mateo, Knutsen et al. 2017, Drew, Mateo et al. 2020). Still, how these oscillations organize at the macroscopic level and their relationship to 'functional connectivity' between brain areas remains unclear.

Intrinsic networks analogous to the ones identified in humans have been identified in rats and to be modulated by the sedation/anesthesia state (Weber, Ramos-Cabrer et al. 2006, Nasrallah, Tay et al. 2014, Paasonen, Stenroos et al. 2018, Gutierrez-Barragan, Basson et al. 2019, van Alst, Wachsmuth et al. 2019). In particular, sedation with low doses of medetomidine has been shown to reveal consistent intrinsic networks but also to drive abnormal high amplitude oscillations in fMRI signals at frequencies extending beyond 0.1 Hz (Thompson, Pan et al. 2014, Paasonen, Stenroos et al. 2018). The addition of isoflurane at low concentrations suppresses these 'high frequency' oscillations while maintaining the typical human resting-state frequencies < 0.1 Hz, such that the combination medetomidine/isoflurane (MED/ISO) is currently the state-of-the-art protocol to approximate 'resting-state' brain activity in rats (Grandjean, Schroeter et al. 2014, Pradier, Wachsmuth et al. 2021).

The solid evidence from rat experiments across sedation/anesthesia protocols offers an ideal setting to analyze the spatiotemporal organization of fMRI signal oscillations and their relationship with intrinsic network patterns(Grandjean, Schroeter et al. 2014, Wu, Mishra et al. 2016, Bukhari, Schroeter et al. 2017). However, the precise characterization of oscillations across space and over time is complex and benefits from an adequate spatiotemporal resolution and high signal-to-noise (SNR) ratio to adequately capture

transient phase-relationships between voxels. Ultra-high field fMRI studies in rats achieve increased SNR by attenuating thermal noise using cryogenic coils(Ratering, Baltes et al. 2008, Arbabi, Noakes et al. 2022). Moreover, for increased precision in the characterization of oscillatory signals, long scanning times are needed to ensure high frequency specificity at slow frequencies, and fast sampling helps preventing frequency aliasing from undersampled periodic components of physiological and/or scanner artifacts. At the spatial level, a large field of view is necessary to capture macroscale organization, while ensuring a sufficient spatial resolution to resolve distinct brain regions.

Therefore, we harness an ultrafast ultrahigh field fMRI approach, with long scan durations of 10 minutes sampled at 38 milliseconds (16000 frames per scan) resolution to characterize the spatial organization of oscillations detected in fMRI signals in a single slice of the rat brain, achieving high SNR ratio via a 9.4 Tesla magnetic field and a cryogenic coil. This approach exposes unreported features of rat brain activity, providing insights into the fundamental organizing principles driving long-range functional connectivity in the brain.

Results

Long range functional connectivity

A typical seed-based functional connectivity analysis was performed to confirm the detection of long-range correlations in fMRI signals in the range of frequencies typically considered in resting-state studies, i.e., ranging between 0.01 and 0.1 Hz **Figure 1 (a-b)**. In panel c, we plot the band-pass filtered fMRI signals in the same 3 seeds together with their contralateral voxels (cf. Supplementary Figure S1 for the corresponding brain atlas). When applying sliding-window correlation (SWC) analysis, fluctuations were detected between sustained periods of positive correlation (yellow shades) and periods of weak or even negative correlation (orange to magenta shades). The same analysis was applied to a scan

from a post-mortem rat to ensure that the periods of sustained correlations are detected at levels beyond any conceivable artifacts (Supplementary Figure S2).

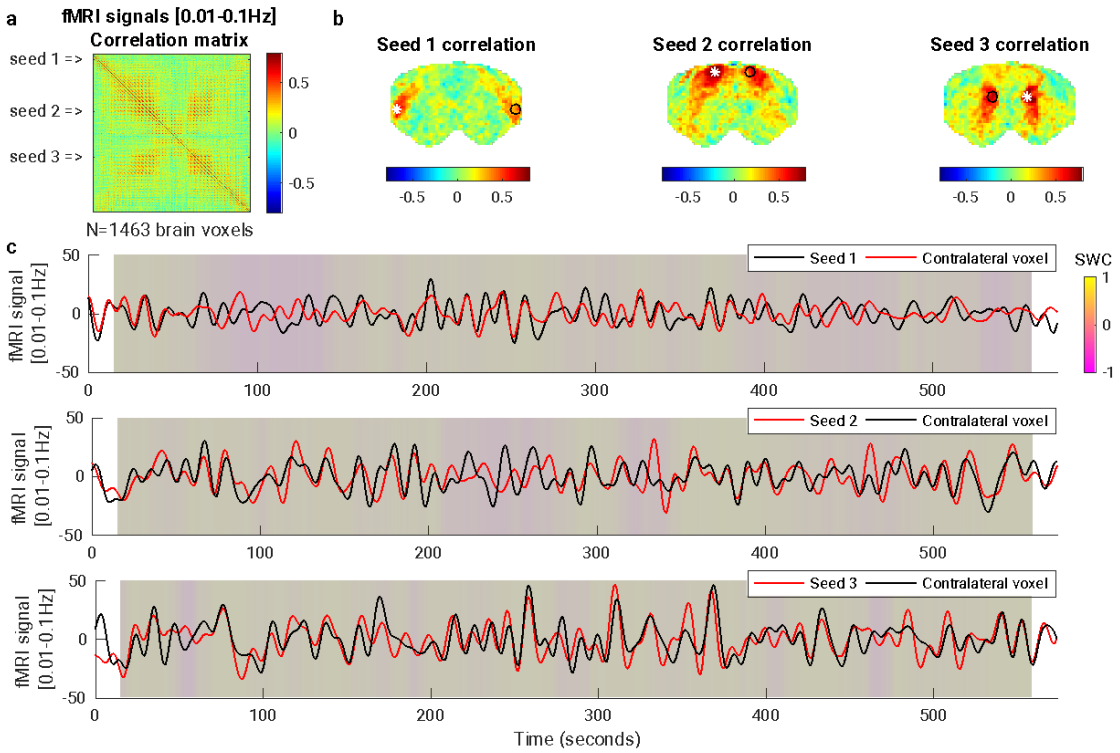

Figure 1 – Static and dynamic resting-state functional connectivity analysis in band-pass filtered fMRI signals. ***(a)*** *Correlation matrix of the fMRI signals in all voxels within the brain mask, bandpass filtered in a range typically considered in resting-state studies, i.e., 0.01-0.1Hz (no nuisance regressor nor spatial smoothing applied). Each line/column in the matrix corresponds to the correlation map of each voxel.* ***(b)*** *Seed-based correlation maps are represented for 3 different seeds (white asterisks), where each voxel is colored according to its degree of correlation with the seed. A voxel contralateral to each seed is represented by a black circle. All colorbars are truncated between -0.8 and 0.8.* ***(c)*** *Filtered fMRI signals recorded in each seed (red) and corresponding contralateral voxel (black). Colored shades represent the sliding window correlation (SWC) using a 30-second window, showing that correlation is not constant but fluctuates between transients of long-range phase locking. The same figure obtained from a postmortem scan is reported in SI figure S1.*

Space-frequency analysis of fMRI signals across conditions

To investigate whether the transient correlations are associated with oscillatory phenomena, we turn to analyze the spectrum of frequencies detected in brain voxels across three different sedation/anesthesia protocols: under medetomidine only (which we term *sedation*), after the addition of isoflurane at 1% concentration (*light anesthesia*), and after increasing isoflurane concentration to 3% (*deep anesthesia*) (see Methods for details). Applying a space-frequency analysis on 36 ultrafast fMRI scans (12 per condition, each 10

minute long at 26.3 Hz sampling rate), the 3 different conditions are compared in terms of power at different frequency bands and across brain voxels with respect to a baseline defined from postmortem scans (**Figure 2**). Power at frequencies up to 0.30 Hz – extending well beyond the range typically considered in resting-state studies - is detected in the brains of sedated and lightly anesthetized rats significantly above deep anesthesia levels (**Figure 2**b).

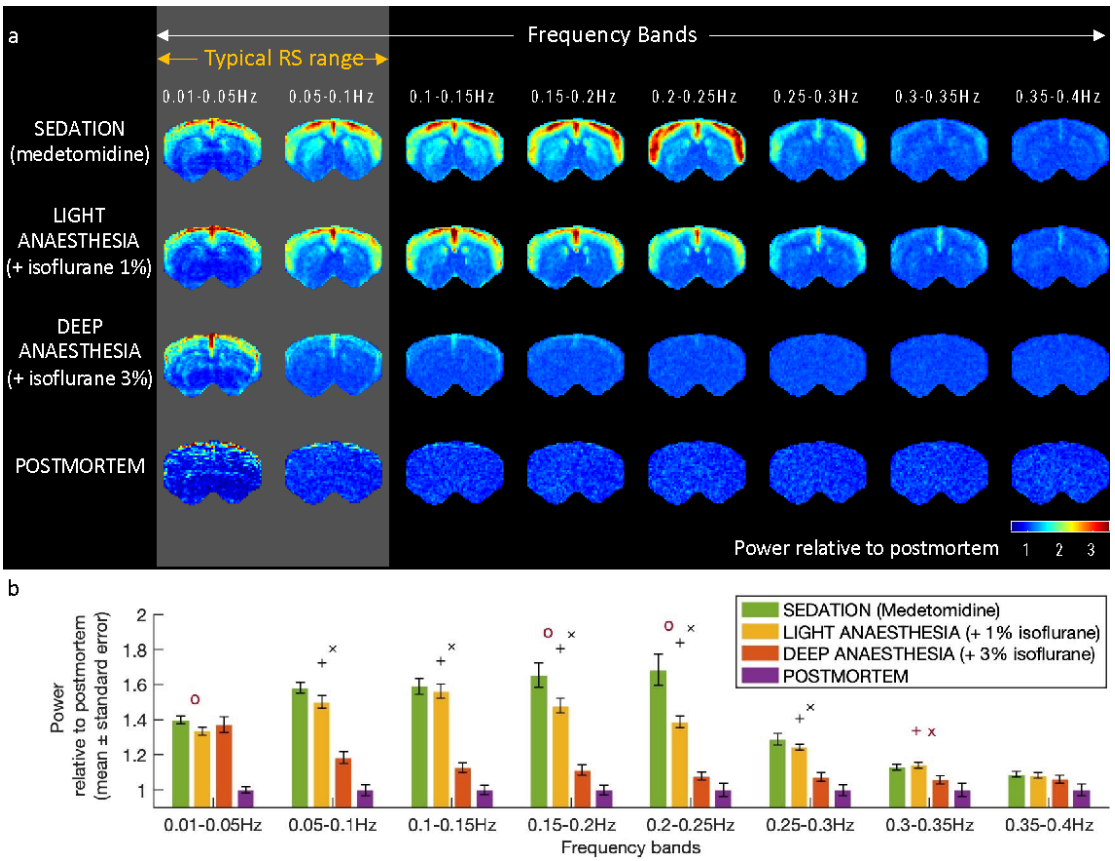

***Figure 2 – Spectral power of the fMRI signals in each brain voxels changes in each condition consistently across rats. A** – Spatial maps of spectral power averaged across all fMRI signals recorded from a frontal brain slice in each condition (power averaged across 12 scans/condition and normalized by the mean power in postmortem scans). **B** – Power across the 12 scans in each condition and in each frequency band relative to the mean power in postmortem scans. Error bars represent the standard error across scans in each condition. Symbols indicate statistical significance between: 'o' sedation vs light anesthesia; '+' sedation vs deep anesthesia; 'x' light vs deep anesthesia. Black symbols indicate Bonferroni-corrected p-values for both the number of conditions and frequency bands compared (p<0.05/3/8), while red symbols survive correction only for the number of conditions compared (p<0.05/3). **RS**, resting-state.*

Power in fMRI signals is found to peak within well-defined cortical boundaries consistently between 0.20 and 0.25 Hz in rats sedated with medetomidine (**Figure 2**). Voxels in the striatum (subcortical) are found to exhibit power at frequencies peaking between 0.1

and 0.15Hz. The addition of isoflurane at 1% is found to specifically affect the power of fMRI signal fluctuations between 0.15-0.25Hz, whereas isoflurane at 3% significantly decreases the power in the broad frequency range between 0.05 and 0.3Hz (**Figure 2**b and Supplementary Figures S3-S6). Above 0.40 Hz, only signatures associated with cardiac and respiratory frequencies are detected (Supplementary Figure S7 and Table S1). Ultra-slow fluctuations below 0.05 Hz, i.e., with a period longer than 20 seconds, persist even in deeply anesthetized animals.

Spatial, temporal, and spectral properties of principal components

While the space-frequency analysis provides information about which voxels have more power in each frequency band, it does not reveal how the signals evolve in time or organize in space. As can be seen in **Video 1**, fluctuations are not globally correlated, but instead exhibit complex phase relationships across space that appear recurrent over time and consistent across different rats in the same condition. Signals co-varying in phase across distant voxels symmetrically aligned with respect to the vertical midline point to a link with long-range functional connectivity. In deep anesthesia, despite applying exactly the same filtering, no particular spatial organization or fine structure is detected except for ultra-slow globally correlated fluctuations.

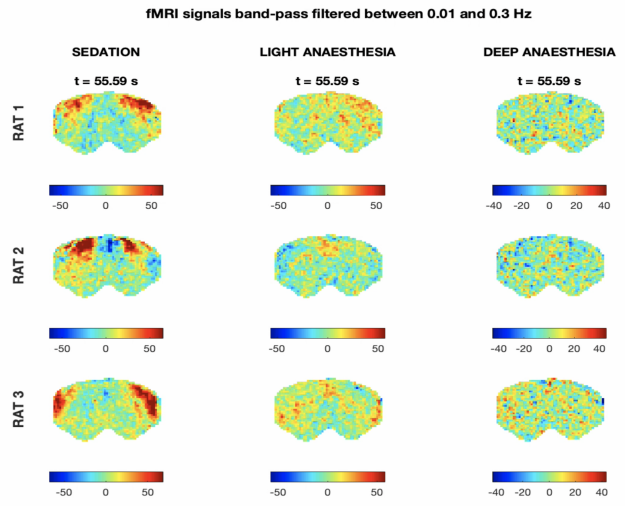

Video 1 (still image)– fMRI signals band-pass filtered between 0.01 and 0.3 Hz in 3 different rats and in 3 different conditions (*Sedation: Medetomidine only; Light Anesthesia: Medetomidine + 1% isoflurane; Deep anesthesia: Medetomidine + 3% isoflurane). To account for expected differences in power across conditions, colorbar limits are set to ±4 standard deviations of the band-pass filtered signals in each scan.*

To characterize whether the fluctuations have a characteristic spatial organization, we extract the principal components of the fMRI signals filtered below 0.3Hz in each condition (e.g., the eigenvectors of the covariance matrix, see **Figure 3** and Methods for details). Principal component analysis has the advantage of returning orthogonal modes of covariance without making any assumption regarding the oscillatory properties of the components, unlike other decomposition techniques that a priori assume an oscillatory nature of the components, such as dynamic decomposition analysis (Schmid 2010, Casorso, Kong et al. 2019). The spatial patterns associated with the 10 principal components detected above postmortem baseline reveal spatially fixed phase relationships between the fMRI signals in distinct brain subsystems (**Figure 3d**). These phase-relationships varying gradually and symmetrically across space exhibit characteristics of standing waves, where regions of strong amplitude (red/blue) represent the 'anti-nodes' of the wave, whereas regions of low amplitude between anti-nodes (green) represent the wave's nodes (points of no motion).

To investigate the dynamic behavior of the principal components, we subsequently analyze the temporal signatures associated with each spatial pattern. In particular, we aim to verify the existence of periodicity between positive and negative representations of the spatial patterns (**Figure 3d**), which is not necessarily a property of principal components, given that signals can co-vary aperiodically. The temporal signature $\tau_{\alpha}^{S}(t)$ of each principal component α for each scan *S* is obtained by performing a matrix multiplication that contracts the 'n' dimension as: $\tau_{\alpha}^{S}(t) = \psi_{\alpha}(n)\,\Psi^{S}(n,t)$, where $\psi_{\alpha}(n)$ represents the spatial pattern of each principal component α and $\Psi^{S}(n,t)$ represents the activity recorded with fMRI across all voxels *n* and timepoints *t* for scan *S* (Figure 3).

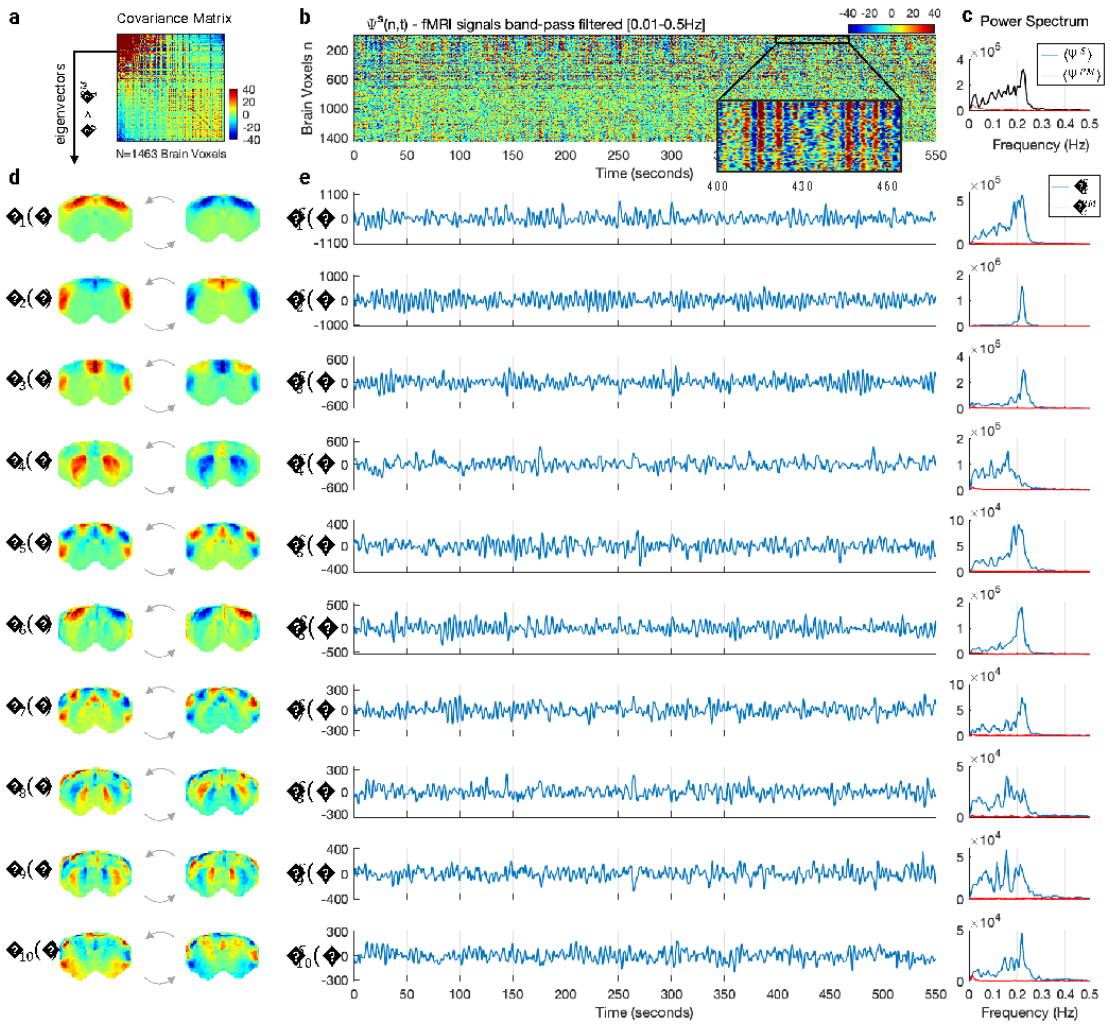

***Figure 3 – Spatial, temporal, and spectral signatures of the principal components in medetomidine-sedated rats. a** – The NxN covariance matrix of fMRI signals (filtered within the range where significant spectral power was detected in the cortex, i.e., between 0.01 and 0.3Hz) averaged across the 12 sedated rat scans. **b** – Carpet plot of the fMRI signals in all brain voxels, n, over time, t, represented by the wave function $\Psi^S(n,t)$, here shown for a representative scan **S** of a sedated rat in the frequency range [0.01-0.5Hz]. Voxels are sorted according to the elements in the largest magnitude eigenvector ψ_1. Values correspond to fMRI signal change with respect to the mean in each voxel. A zoom into the first 100 voxels over 60 seconds is inserted to illustrate oscillations in the signals. **c** – Power spectrum of the mean fMRI signal across voxels for: (black) the scan shown in **b** and (red) a scan performed postmortem (**PM**). **d** – The 10 principal components ψ_α obtained as the eigenvectors from (**a**) with eigenvalue λ_α above PM baseline are scaled by 1 (left) and -1 (right) to illustrate the activity pattern when the temporal signature oscillates between positive and negative values. **e** – Temporal signature associated to each of the 10 principal components given by $\tau_\alpha^S(t) = \psi_\alpha(n)\Psi^S(n,t)$ for the same scan shown in **b**. Clear oscillations with fluctuating amplitude can be observed. **f** – Power spectra of the temporal signatures from **e** (blue) and in a postmortem scan (red)**.** See Video 2 to observe the behavior of each principal component over time.*

The reconstruction $\Psi^R(n,t) = \sum_\alpha \psi_\alpha(n)\tau_\alpha^S(t)$ describes the linear superposition of a basis of wave patterns locked in space $\psi_\alpha(n)$ and evolving in time $\tau_\alpha^S(t)$. Video 2 illustrates how the essential macroscopic dynamics of the recorded fMRI signals in a rat brain are

captured using a low-rank approximation considering only the reduced common basis of 10 principal components $\psi_{\alpha}(n)$ detected across sedated rats, and the 10 scan-specific temporal signatures $\tau_{\alpha}^{S}(t)$ associated with these components. As observed in **Figure 3** and **Video 2**, the principal components are found to oscillate around the mean with slowly fluctuating amplitudes, generating patterns akin to those of transiently resonating stationary waves.

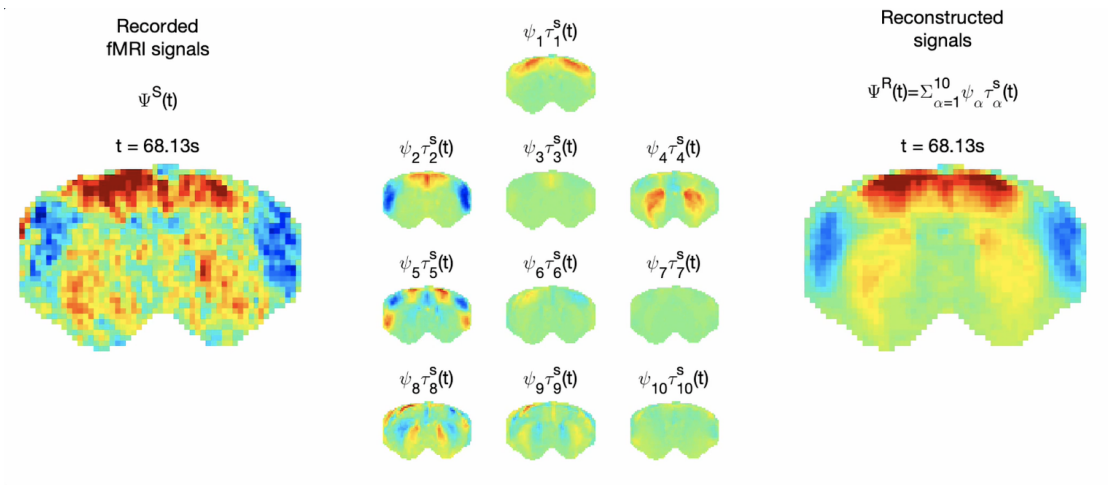

Video 2 (still image)– Reconstruction of a representative fMRI recording as the superposition of 10 condition-specific principal components with scan-specific temporal signatures. (left) *fMRI signals band-pass filtered between 0.01 and 0.3 Hz recorded from a representative rat under medetomidine only.* ***(middle)*** *Each of the 10 principal components obtained from the covariance matrix averaged across all 12 sedated rat scans is scaled by the associated scan-specific temporal signature.* ***(Right)*** *To account for differences in power across components, colorbar limits are set to ±4 standard deviations of the temporal signatures.*

The detection of oscillations associated with the spatial patterns benefited from the fast sampling combined with long scan durations (totaling 16000 images per 10 minute scan), by preventing frequency aliasing from physiological rhythms (i.e., with Nyquist frequency above breathing and cardiac frequencies) and by ensuring sufficient resolution in the power spectrum at low frequencies, i.e., with precision below 0.01 Hz (see Supplementary Figures S10-11). As shown in **Figure 4** (top row), when projecting the *1xN* spatial component (here $\psi_{\alpha=7}$) on the *NxT* ultrafast unfiltered fMRI signals, the temporal signature $\tau_{\alpha=7}^{S}$ exhibits clearly visible oscillations between positive and negative

representations of the spatial pattern. As the sampling factor is increased, even if a resonant peak frequency can still be detected, the signal to noise ratio is decreased. Indeed, we find that the principal component $\psi_{\alpha=7}$ fails to be detected with a sampling as fast as 380 ms, which coincides with the sampling rate at which the breathing frequency (~2 Hz) cannot be adequately resolved given the Nyquist theorem (analysis shown in Supplementary figures S12-S16). In Supplementary Figure S15 we reorder the spatial patterns and demonstrate that the temporal signatures are specific to the spatial organization of the phases.

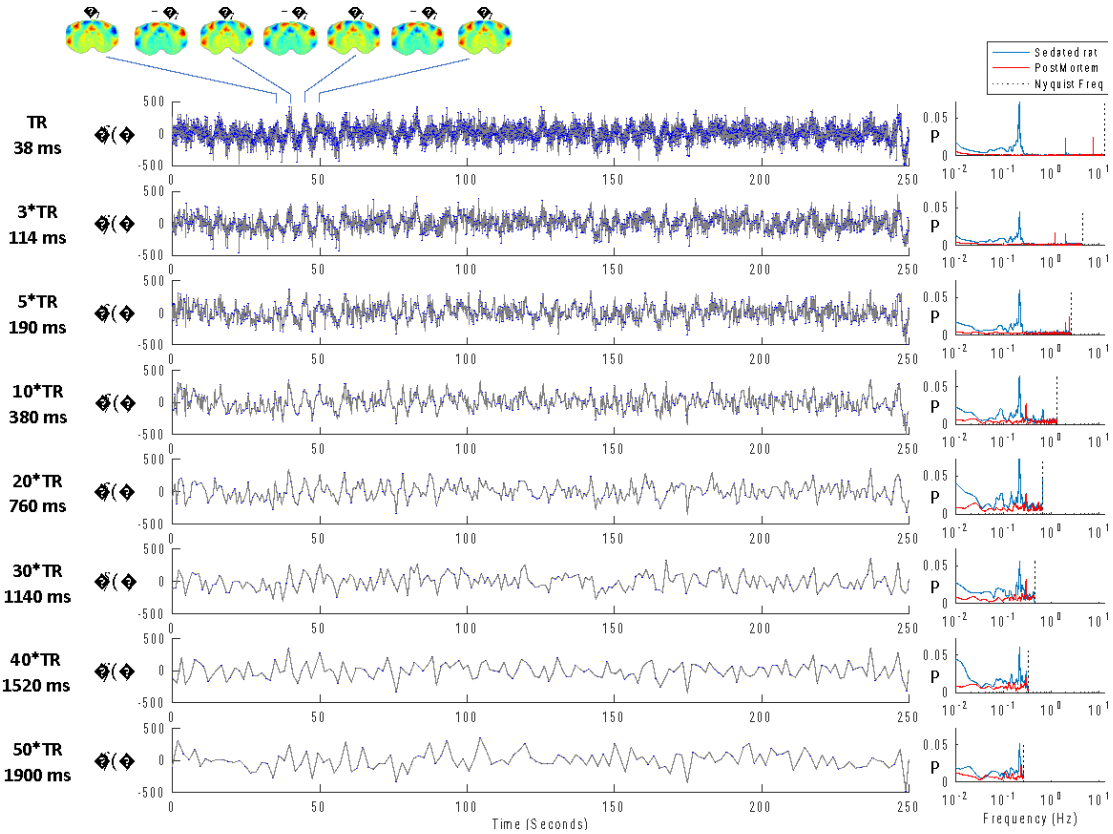

Figure 4 – Effect of the sampling rate in the power spectrum given a fixed scan duration. Left*: The unfiltered temporal signal $\tau_7^S(t)$ associated with the 7th principal component detected in ultrafast fMRI signals from medetomidine-sedated rats (Time of Repetition, TR= 38 milliseconds, ms) is downsampled by considering only one in every 3, 5, 10, 20, 30, 40 and 50 frames (corresponding to intervals of 114, 190, 380, 760, 1140, 1520 and 1900 ms between frames). Plots shown for 250 seconds from a representative scan **S** (same from **Figure 3**). **Right:** The power spectral density (PSD) of the sampled signals computed for scan **S** (blue) and for a scan performed postmortem (red). For each downsampling factor, both PSD (red and blue) are normalized by the total power in the postmortem scan. PSD are computed over the entire scan duration of 590 seconds.*

With the addition of isoflurane at 1% concentration (**Figure 5** top), the repertoire of principal components is modified, not only in number - with only 6 components detected

above the postmortem baseline - but also in terms of spatial configuration, with different brain subsystems oscillating in phase or anti-phase with each other. Regarding the temporal signatures associated with the different components, although some transient oscillations can still be detected, these last visibly shorter and with different periodicity over time (**Figure 5e)**, which is reflected in a broader distribution of power across the spectrum, peaking at lower frequencies with respect to the sedation condition (**Figure 5f)**.

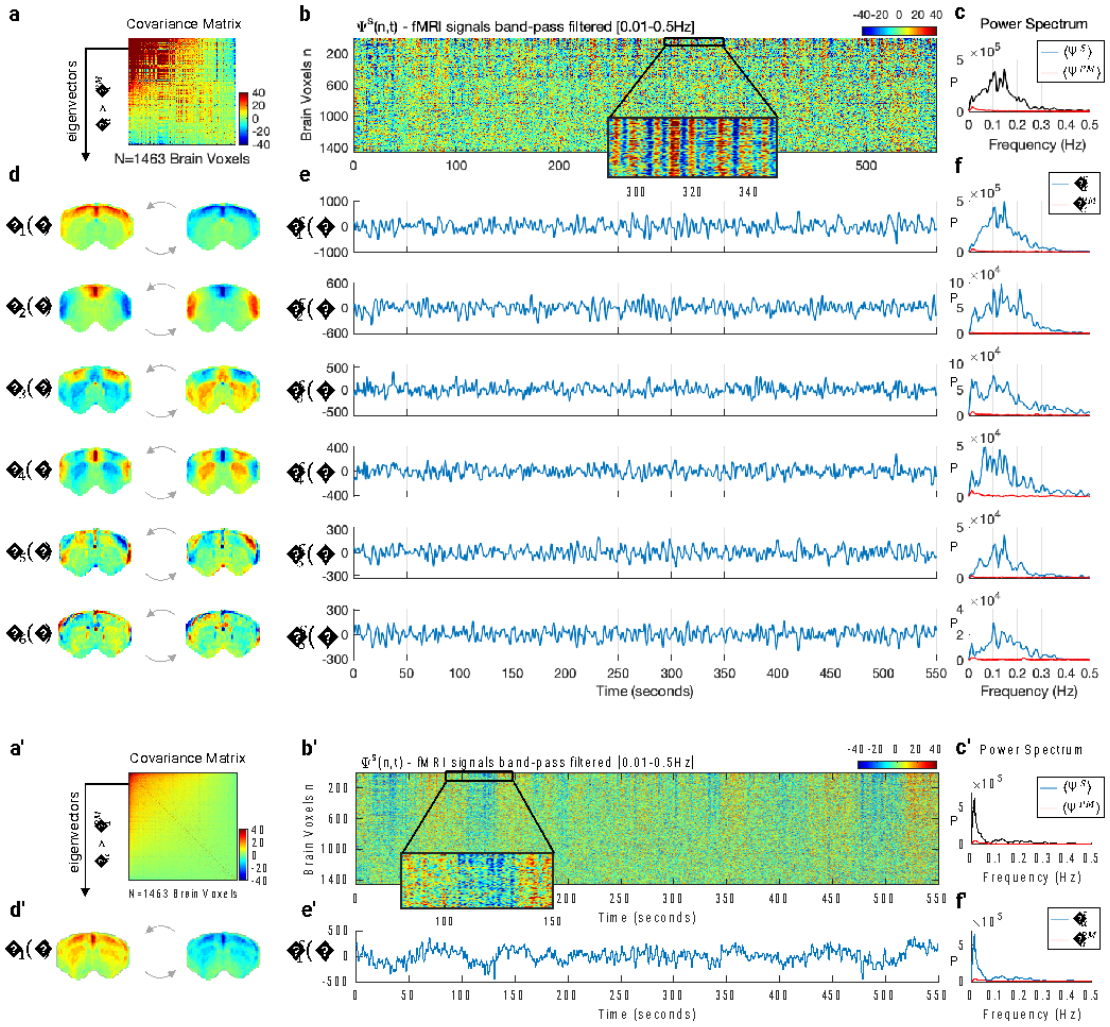

Figure 5 – The addition of isoflurane at 1% and 3 % concentrations alters the spatial, temporal, and spectral signatures of principal components. (a,a') *The NxN covariance matrix of fMRI signals band-pass filtered between 0.01 and 0.3Hz, averaged across 12 scans after the addition of isoflurane at 1%* ***(top)*** *and 3%* ***(bottom)*** *concentrations.* ***(b,b')*** *Carpet plot of the fMRI signals recorded in all brain voxels, n, over time, t, represented by the wave function* $\Psi^S(n,t)$*, here shown for two scans S of the same rat from Figure 3 in the frequency range [0.01-0.5Hz]. Voxels are sorted according to the elements in the largest magnitude eigenvector* ψ_1*. Values correspond to fMRI signal change with respect to the mean in each voxel. A zoom into the first 100 voxels over 60 seconds is inserted to illustrate oscillations in the signals.* ***(c,c')*** *– Power spectrum of the mean fMRI signal across voxels.* ***(d,d')*** *The principal components detected with eigenvalue above baseline are scaled by 1 (left) and -1 (right) to illustrate the activity pattern when the temporal signature oscillates between positive and negative*

values. ***(e,e')*** *Temporal signature associated to each of the supra-threshold principal components given by* $\tau_{\alpha}^{S}(t) = \psi_{\alpha}(n)\Psi^{s}(n,t)$ *for the same scan shown in* ***b****.* ***(f,f')*** *Power spectra of the temporal signatures from* ***e.***

When the concentration of isoflurane is further increased to 3% (**Figure 5** bottom), the variance above postmortem baseline is explained by a single principal component where the cortex and striatum oscillate together in phase (**Figure 5**d') and at very low frequencies (**Figure 5**f'). These ultraslow global fluctuations are particularly visible in the carpet plot in **Figure 5**b'.

The oscillatory nature of principal components

While in Figures 3 and 5 we show the results from one representative animal, in **Figure 6** we report the peak frequency and stability of the oscillations associated with each principal component in each of the 36 scans, i.e., for the 6 rats scanned twice in each condition. The stability of the oscillations is assessed from the resonance Q-factor, which is proportional to the number of cycles before the amplitude decays to ~37% (e^{-1}) of its initial value, consisting the ratio between the peak frequency and the power spectrum's full-width-at-half-maximum (FWHM). Both the peak frequencies and the Q-factors were found to be significantly higher (and with larger variability across scans) in sedation and light anesthesia with respect to deep anesthesia (Bonferroni-corrected p-values reported in Supplementary Table S2).

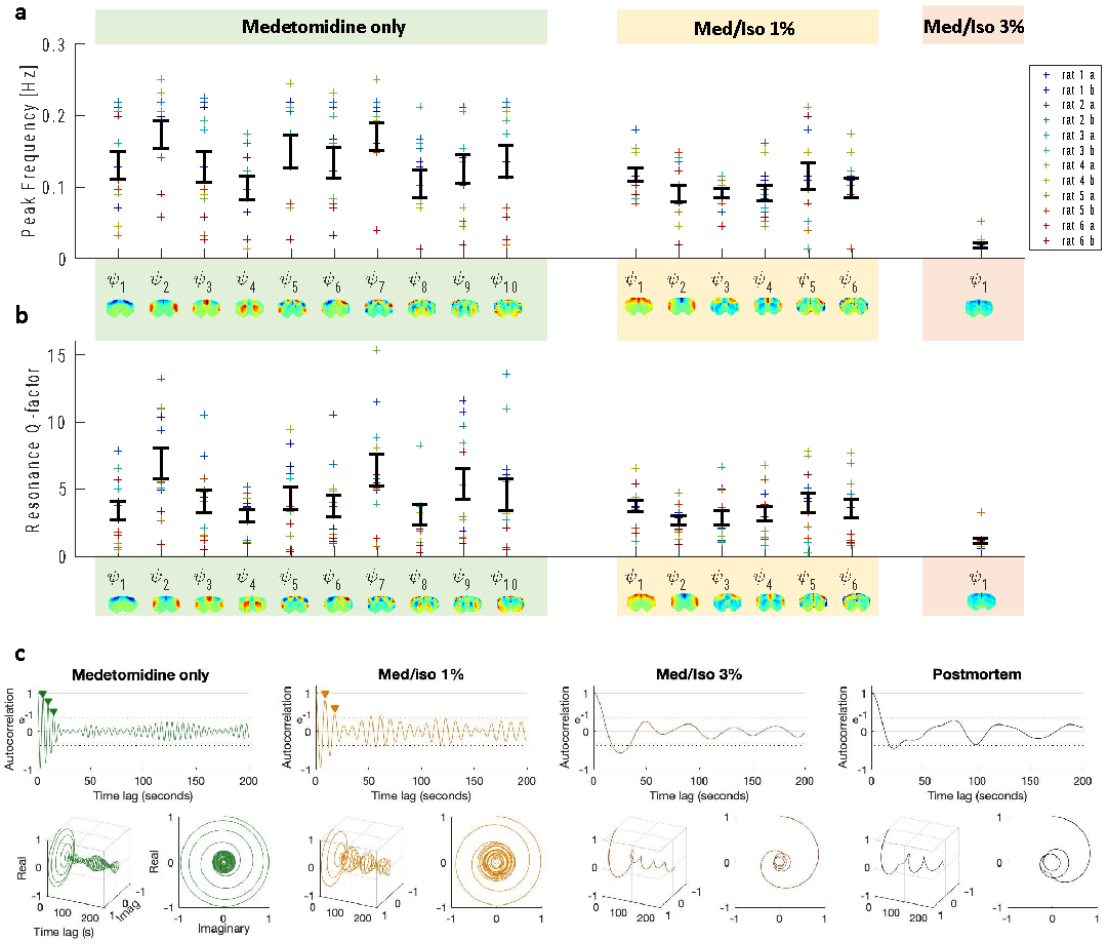

Figure 6 – Principal components oscillate at higher frequencies and with less damping under medetomidine. (a,b) *The temporal signatures associated to the principal components detected in each condition are characterized in terms of peak frequency and Q-factor for each of the 12 scans in each condition (2 scans per rat per condition). Error bars represent the mean ± standard error across scans.* ***(c)*** *To illustrate the stability of the oscillations, the autocorrelation functions of the temporal signatures* τ_1^S *associated to the first principal component in each condition are reported. Examples are shown for 3 scans from the same rat and from a postmortem scan. As can be seen, the autocorrelation function under medetomidine exhibits 3 oscillations before the amplitude decays to 1/e (~37%), 2 cycles after adding isoflurane at 1% and no complete cycle under deep anesthesia, similar to what is observed in the postmortem scan.*

The autocorrelation functions of the wave temporal signatures (here shown for $\tau_1^S(t)$ in each condition) illustrate that the number of sustained cycles before the amplitude decays to 1/e decreases with increasing levels of isoflurane, as estimated by the Q-factor (**Figure 6**c). We use the Hilbert transform to obtain a representation of the autocorrelation functions in complex domain (with real and imaginary components) and plot the corresponding phase portraits (**Figure 6**c bottom). The representation of the phase portraits serves to classify the temporal signatures of the components within the framework of dynamical systems stability

theory, demonstrating that the components have a 'spiral sink' trajectory back to equilibrium according to the Poincaré diagram (Teschl 2012).

Stochastic resonance of standing waves

The presence of a spiral sink in the autocorrelation function of a dynamical system is indicative of underdamped oscillatory motion, where the system returns to a fixed point equilibrium upon perturbation with an oscillation with decaying amplitude. An underdamped system will resonate at its natural frequency either when perturbed at its natural frequency or in the presence of background noise due to stochastic resonance (see Supplementary Figure S16 for an illustration).

Given that the principal components detected in rat brain activity have spatial features of standing waves (in line with previous studies) and, as we demonstrate here, exhibit transient oscillations over time, it can be hypothesized that their phenomenology is associated with the stochastic resonance of standing waves. In such a mechanistic scenario, the differences detected across conditions can be further hypothesized to be related with alterations in the properties of the medium through which the waves propagate, while the anatomical structure remains unchanged. Indeed, while medetomidine is found to increase the number, peak frequency and Q-factor of resonant modes, isoflurane is found to gradually dampen the resonant modes of the system, with only global aperiodic fluctuations being detected under deep anesthesia (Figure 6).

To demonstrate that the stochastic resonance of stationary wave patterns can generate the patterns of intrinsic functional connectivity observed experimentally, we model the signals in the brain slice as the superposition (i.e., linear sum) of modes whose spatial configuration $\psi_{\alpha}(n)$ is fixed and given by the principal components detected empirically, and

the temporal signature $Z_\alpha(t)$ is obtained using the Stuart-Landau equation to simulate the behavior of an oscillator in the underdamped regime in the presence of background noise as:

$$\Psi^{Model}(n,t) = \sum_\alpha \psi_\alpha(n) Z_\alpha(t),$$

with

$$dZ_\alpha/dt = Z_\alpha(i\omega_\alpha - |Z_\alpha|^2 + a) + \beta\eta,$$

where ω_α is the resonant frequency of each mode, a (negative) scales the decay rate and η is the added gaussian white noise η with standard deviation β.

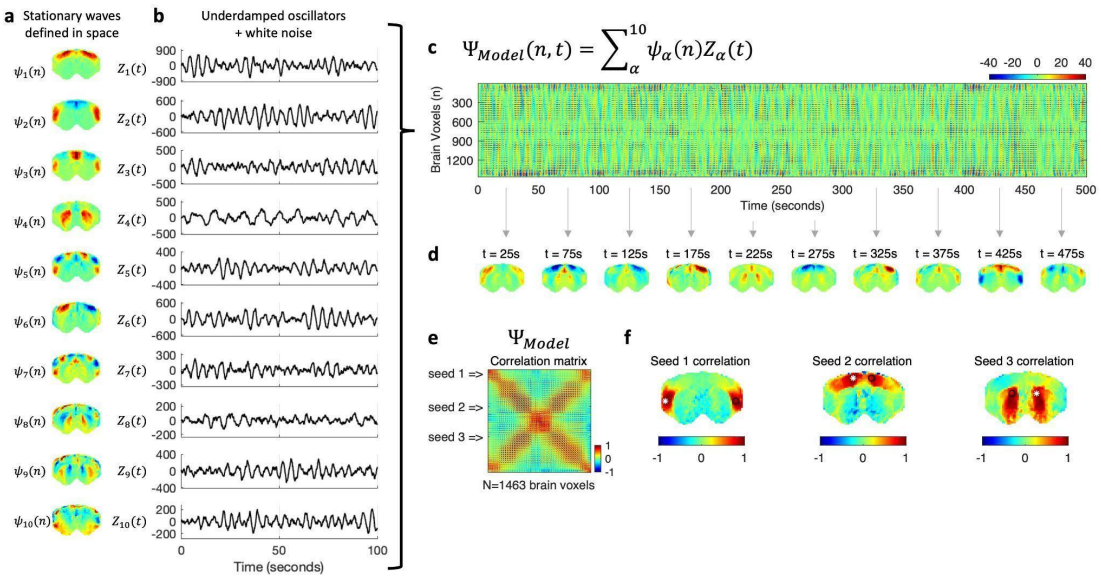

Figure 7 – Stochastic resonance of standing waves drives transient long-range correlations in simulated signals. *The spatial configurations and temporal signatures of the principal components align with the hypothesis that they represent standing waves, whose phenomenology is inherently associated with resonance phenomena. To model the dynamics emerging from the transient resonance of standing waves in the presence of background noise, we simulate a temporal signature for each of the spatial patterns detected in medetomidine sedated rats (**a**) as the behavior of an underdamped oscillator perturbed with gaussian white noise, with natural frequency fitted to the peak frequency obtained from one representative scan, and fitting the standard deviation to the temporal signatures of the same scan (**b**). Multiplying the Tx1 temporal signatures by the corresponding 1xN spatial patterns and summing across modes results in a NxT spatiotemporal pattern representing the result from the stochastic resonance of a repertoire of standing waves.*

As shown in Figure 7, the stochastic resonance of a repertoire of standing waves (here considering the repertoire detected empirically in sedated animals) results in a spatiotemporal pattern sharing features with what is detected from fMRI recordings. This

model includes the possibility to tune the oscillators in the overdamped regime, in which case it can approximate the results obtained in deeply anesthetized animals, where no resonant oscillations are detected but only aperiodic fluctuations. In other words, the model of stochastic resonance does not exclude the hypothesis of scale-free fluctuations driving the fMRI signals, but it considers it to be a particular case where the oscillatory modes are overdamped.

In Figure 7d, we show snapshots of activity generated from the superposition of standing waves resonating in the presence of background noise to illustrate the multiplicity of patterns that can be generated at the instantaneous level, as observed in empirical recordings. Finally, to link with long-range functional connectivity, we compute the correlation matrix of the simulated signals, demonstrating that the stochastic resonance of standing waves is a possible mechanism to generate correlations between contralateral brain regions located at the wave antinodes.

Expansion to the whole-brain level

To expand our results obtained in a single slice to the whole-brain level, the principal components were obtained from six 15-minute-long fMRI scans covering 12 brain slices of 3 rat sedated with medetomidine. Despite the necessarily lower temporal resolution of multi-slice acquisitions (here TR= 350 ms), oscillations could still be visually observed (see Video 3), organizing with phase relationships that overlap (in slice 6) with the ones detected in the frontal slice of ultrafast fMRI recordings, supporting the hypothesis that the conclusions drawn from the single slice ultrafast acquisitions can be expanded to the whole-brain level (Supplementary Figures S17-S19). However, although consistent principal components were detected at the spatial level (the first 5 are rendered in a transparent brain in Figure 8a), the limited temporal resolution and the added artifacts resulting from multi-slice acquisitions were found reduce the sensitivity to transient oscillations such that

even in the fMRI scan that exhibited most power > 0.15 Hz, the sensitivity to frequency-specific oscillations is much lower than the one observed in single-slice acquisitions (Supplementary Figure S19).

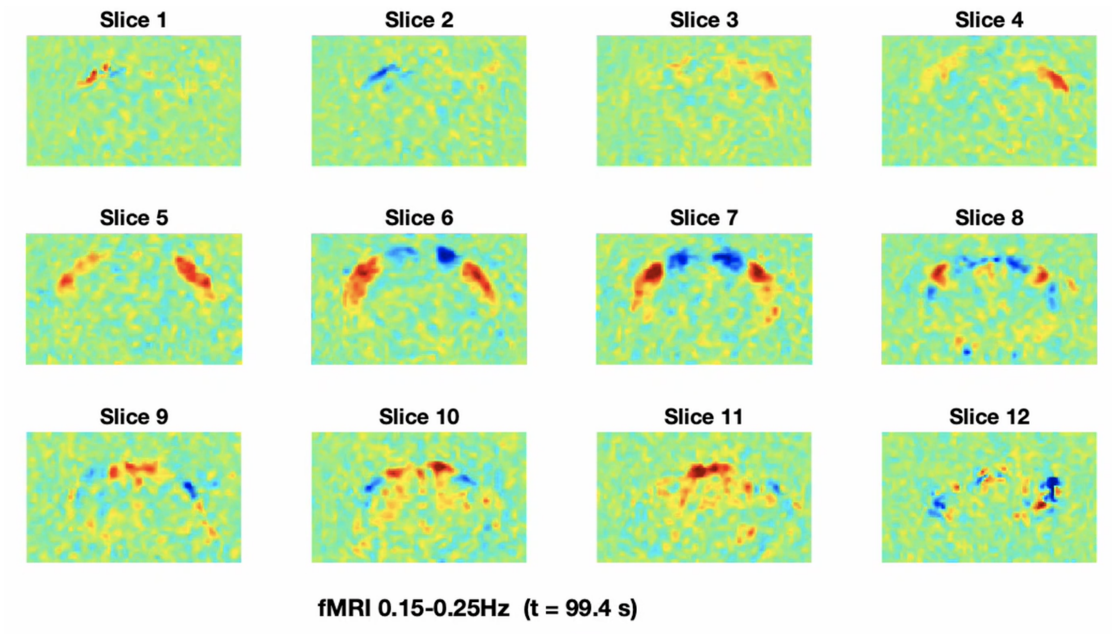

Video 3 (still image) – Multi-slice acquisitions reveal that the patterns detected in the frontal slice extend to the whole brain level. *fMRI signals recorded from a rat sedated with medetomidine with TR=0.350 seconds from 12 slices covering the whole brain (anterior to posterior) filtered between 0.15-0.25 Hz (no other signal processing performed).*

In summary, our experiments revealed that: i) power at frequencies extending up to 0.3Hz is consistently detected in the fMRI signals from rat brains, peaking in power in the cortex of rats sedated under medetomidine; ii) fMRI signal fluctuations organize into a discrete repertoire of modes with fixed phase relationships across space; iii) high sampling rates allow detecting transient fine-tuned oscillations in the modes' temporal signatures; iv) the oscillatory modes are sensitive to anesthesia varying both in number, frequency, stability and spatial configuration; v) the oscillatory modes detected exhibit features of a dynamical system operating in the subcritical range of a Hopf bifurcation; vi) the stochastic resonance of stationary patterns generates patterns of long-range functional connectivity similar to the ones detected empirically; vii) These findings support the emerging hypothesis that

resting-state activity detected with fMRI results from the superposition standing waves emerging from resonance phenomena within the brain's anatomical structure, which in turn drive fluctuations in sliding-window correlations between the brain subsystems located at the wave antinodes (Figure 8b).

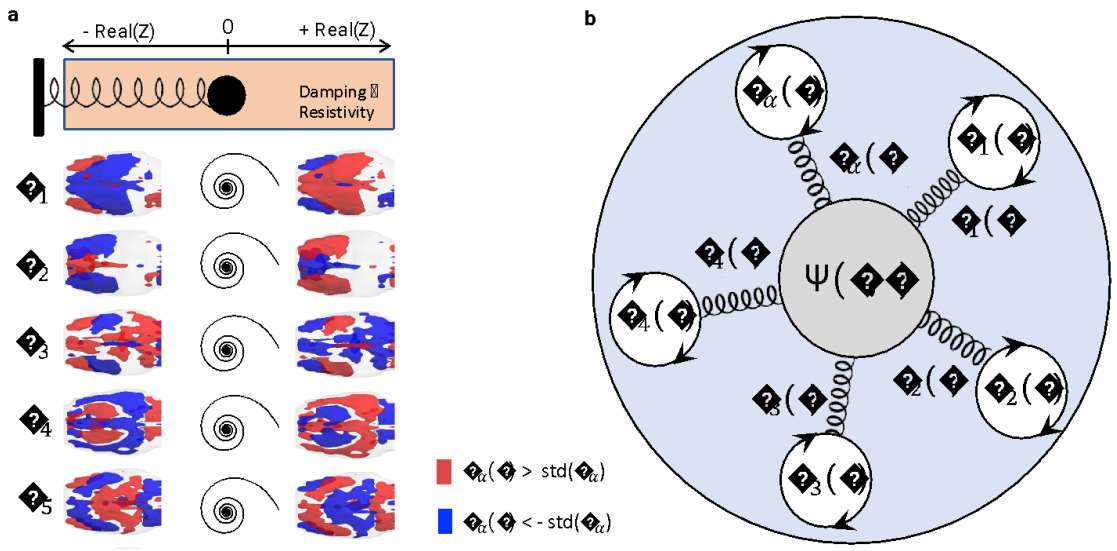

***Figure 8 – Mechanistic model for the spontaneous resonance of standing waves driving the activation of functional brain networks. D** — Diagram illustrating a mechanistic scenario for brain activity, where each functional network is represented by a spatial pattern ψ_α responding to perturbation with a damped harmonic motion. **E** - Like the response of a spring, the temporal signature of brain modes can be approximated by a damped oscillator. Despite the lower temporal resolution inherent to multi-slice acquisitions hindering the detection of resonant behavior, the consistency of spatial patterns reinforces the hypothesis that the damped oscillatory response of functional networks extends to the whole-brain level, here represented by the first 5 eigenvectors of the average covariance matrices across 6 whole-brain scans (from 3 different rats).*

Discussion

Rhythms at frequencies ranging from 0.5 up to >100 Hz have been shown to emerge from intrinsic neural processes (Engel, Fries et al. 2001, Buzsáki 2006, Wang 2010). However, the role and generative mechanisms of rhythms below 0.5 Hz detected both with fMRI, EEG and electrophysiology remain under vigorous debate (Breakspear 2017, Cabral, Kringelbach et al. 2017, Drew, Mateo et al. 2020, Pradier, Wachsmuth et al. 2021, Henderson, Aquino et al. 2022). Using fMRI experiments with hitherto unprecedented spatiotemporal resolution we provide new insights into this problem by demonstrating the existence of intrinsic macroscale oscillatory modes in fMRI signals, which organize with mode-specific phase relationships across extended areas across the cortex and subcortex, driving correlated activity between distant regions.

The oscillatory modes detected were found to be consistent across rats within the same anesthetic condition, but to vary in terms of spatial configuration, peak frequency and damping coefficient across conditions. Despite these differences, the modes detected across conditions are qualitatively similar in terms of organization through phase gradients within anatomically defined cortical and subcortical boundaries, indicating they likely share a common generative principle. Thus, the new parameters that become accessible when characterizing these intrinsic modes may be beneficial compared with the more conventional 'functional connectivity' or 'dynamic functional connectivity' metrics, as they provide quantitative parameters on the nature of the correlation. It is further worth noting that the snapshots of our intrinsic mode oscillations resemble the spatial patterns exposed by quasi-periodic patterns (QPPs) (Yousefi, Shin et al. 2018, Bolt, Nomi et al. 2022) and co-activation patterns (Gutierrez-Barragan, Singh et al. 2022), which were found to improve the characterization of early Alzheimer's disease stages (Belloy, Shah et al. 2018, van den Berg, Adhikari et al. 2022) compared with more conventional resting-state fMRI functional

connectivity metrics. Extending such characterizations using the Intrinsic macroscopic oscillatory mode framework may shed further light into disease, as well as how activating or silencing specific areas contributes to whole-brain modulations (Zerbi, Floriou-Servou et al. 2019, Rocchi, Canella et al. 2022).

Our results also align with neural field theories for macroscale brain dynamics describing large-scale wave propagation of neuronal activity including a spatial Laplacian to incorporate the brain geometry of the brain (Jirsa and Haken 1996, Robinson, Rennie et al. 1997, Deco, Jirsa et al. 2008, Gabay and Robinson 2017). While these neural field theories have historically been used to describe macroscale brain activity detected with EEG, recent studies suggest that the structural eigenmodes (defined either from brain surface geometry or from diffusion networks) may also be at the origin of macroscopic activity patterns detected with fMRI, namely the so-called 'resting-state networks' or 'intrinsic connectivity networks' (Friston, Kahan et al. 2014, Atasoy, Donnelly et al. 2016, Robinson, Zhao et al. 2016, Tewarie, Abeysuriya et al. 2018, Xie, Cai et al. 2021). This has been recently reinforced by a study demonstrating high spatial similarity between the covariance eigenvectors of fMRI signals and the theoretical prediction of Helmholtz eigenmodes of the Laplace-Beltrami operator starting from a brain surface mesh (Henderson, Aquino et al. 2022). Overall, these studies support our interpretation that the principal components detected empirically from the fMRI signals are eigenmodes intrinsic to the brain structure, including not only the cortex but also subcortical structures, such as the striatum. Indeed, a closer inspection of the spatial configuration of the modes shown in Figure 3 reveals that distinct eigenmodes emerge not only in the cortex but also in the striatum, with some possibly representing fundamental (i.e., global) modes of specific brain structures (i.e., ψ_1 for the cortex and $\psi_4$for the striatum), while others may represent subsequent harmonic modes with increasing spatial frequencies (i.e., $\psi_{6,2,3,5,7}$ for the cortex and ψ_8 for the striatum).

While under medetomidine alone, strong oscillations were detected up to 0.3Hz in agreement with previous literature (Thompson, Pan et al. 2014), the addition of, isoflurane at 1% concentration was found to particularly suppress the power between 0.10 and 0.25 Hz, leaving the power in the typical range considered in resting-state studies (i.e. < 0.1 Hz) mostly unchanged. Further increasing isoflurane concentration to 3%, most oscillatory power is lost and only very slow (<0.05Hz) global and aperiodic fluctuations are detected. It remains unclear whether these non-linear effects are related with the differential effects of medetomidine and isoflurane on blood vessels or can be explained by more direct changes in the resistivity of the medium through which the waves propagate, altering its resonant quality.

The differences detected across anesthetic conditions question the theoretical predictions of modes depending on the brain geometric structure alone, because it is implicit that the anatomy of the brain is invariant across conditions. Indeed, it is generally known that the resonant modes of a system depend not only on the structural geometry of the system, but also on the resistivity of the propagating medium, which directly affects not only the spatial patterns, but also the resonant frequency and the stability of the oscillations. Given that anesthetics directly affect diverse properties of the brain tissue and vasculature, our results raise the importance to consider not only the brain geometry but also the resistivity of the medium through which the waves propagate to possibly explain the differences in resonant quality observed across anesthetic conditions.

Though many models can be used to describe damped oscillatory motion, we find the Stuart-Landau equation in the subcritical range of a Hopf bifurcation to be appropriate since it is the canonical form to describe a system in the vicinity of a limit cycle, responding to perturbation with oscillations with decaying amplitude from basic mathematical principles, with the imaginary component ensuring the conservation of angular momentum

(Ashwin, Coombes et al. 2016). Hopf bifurcation models have been used in models of spontaneous brain activity to represent local field oscillations interacting through the connectome structure(Deco, Cabral et al. 2017, Deco, Cruzat et al. 2019, Cabral, Castaldo et al. 2022). Here instead, we demonstrate that the oscillations detected with fMRI are not purely local since they lock in phase across distinct subsystems and therefore each oscillator model is associated to a distributed spatial map of phase relationships, analogous to the modes of vibration in a violin string or a drum membrane (Sapoval, Gobron et al. 1991, Robinson, Henderson et al. 2021, Henderson, Aquino et al. 2022). We show that the temporal signature of the wave patterns can be approximated by an oscillator model with varying natural frequency and damping coefficients. In such a framework, the less damped the system is, the more it resonates at its natural frequency in the presence of naturally occurring noise. We hypothesize this is what is occurring under medetomidine. If the damping is increased (as observed with the addition of isoflurane), then the oscillations are sustained over fewer cycles and at slower frequencies.

Being inherently associated with resonance, standing waves are a fundamental property of matter, resulting from the constructive interference of waves travelling in opposite directions, driving correlated (and anti-correlated) oscillations in the wave's anti-nodes. The general principle of wave superposition implies that the brain can engage simultaneously in multiple functional networks, instead of switching from one functional network to another, as often considered in the analysis of dynamic functional connectivity(Allen, Damaraju et al. 2014, Hansen, Battaglia et al. 2015, Cabral, Vidaurre et al. 2017, Stevner, Vidaurre et al. 2019). In other words, our results substantiate that the activity recorded herein with fMRI aligns with neural field theories (Nunez 1974, Jirsa and Haken 1996, Nunez and Srinivasan 2014, Henderson, Aquino et al. 2022), where at any given moment, the wave function Ψ - representing the collective systemic activity - results from

the superposition of a discrete set of wave functions with damped oscillatory response. This resonance framework offers simultaneously an explanation for i) the spontaneous emergence of ultra-slow oscillations in brain activity, ii) the profile of phase relationships across space (as observed in gradient-like functional connectivity patterns) and iii) the difference in damping coefficients across conditions.

The generalization of these findings to other animal species including humans can only be discussed in the light of existing literature and needs further experimental validation. On one side, the similarity of the principal components detected herein with intrinsic network patterns detected using different methodologies suggest these are expressions of the same emergent phenomena, typically referred to as 'resting-state networks' (RSNs) or 'intrinsic connectivity networks' (ICNs). Since both rats, mice, monkeys, and humans exhibit qualitatively similar RSNs/ICNs, it can be expected that they are expressions of the same phenomenon. Indeed, a wide range of studies have demonstrated that intrinsic macroscale modes of brain activity (detected across modalities) exhibit spatial features of standing waves, so it can be expected that their temporal signature exhibits a damped harmonic motion. Even if no clear periodicity is detected in resting state fMRI in humans and the fluctuations closely approximate the canonical hemodynamic response function, one cannot exclude the possibility that the fluctuations reflect an overdamped oscillatory response associated with the transient and short-lived resonance of a stationary wave, providing a new generative hypothesis for the dynamic patterns observed empirically.

A question that typically arises in this context is how closely the fMRI signals track the underlying neural activity, mainly due to the involvement of neurovascular coupling mechanisms. Although this study did not attempt to deconfound neural activity from vascular coupling, it is interesting to note that the mode temporal signatures did not follow the canonical hemodynamic response function. Instead, a ubiquitous transiently sustained

periodicity occurs within a range of frequencies extending significantly above the range typically associated with the BOLD signal, but below cardiac and respiratory physiological rhythms. Recent studies combining simultaneous electrophysiological recordings of local field potentials (LFPs) and fMRI in rats reported significant coherence between the two signals precisely in the range of frequencies detected herein (Pan, Thompson et al. 2013, Thompson, Pan et al. 2014). Therefore, one cannot exclude the possibility that the oscillations observed with fMRI are linked with other factors beyond blood flow/volume effects alone, and may provide a more direct measurement of neuronal activity (Lewis, Setsompop et al. 2016, Toi, Jang et al. 2022). Still, given that hemodynamic blurring is expected (Gonzalez-Castillo, J., Saad, Z.S., et al., 2012.) further local spectral properties may have been obscured by this blurring.

The advantages of exploring fMRI signals at faster resolutions extend well beyond this work and certainly deserve further exploration. While previous ultrafast fMRI experiments in rodents have reached up to 20 frames per second, they have focused mostly on stimulus-driven responses in specific regions of interest (Yu, Qian et al. 2014, Yu, He et al. 2016, Kay, Jamison et al. 2020, Lake, Ge et al. 2020, Gil, Fernandes et al. 2021), and much remains to be explored at the level of spontaneous long-range interactions. Allowing for a large span of scales both in space (from micrometer to meter) and in time (from millisecond to hour), exploring the full possibilities of MRI may provide relevant insights into the brain organizational principles in the spatial, temporal, and spectral domains (Toi, Jang et al. 2022). Indeed, the traditionally low temporal resolution of fMRI studies has limited the analysis to spatial correlations between ultra-slow fluctuations in distant areas. More recent dynamic analysis of functional connectivity has revealed the non-stationary nature of network interactions (Hutchison, Womelsdorf et al. 2013, Calhoun, Miller et al. 2014, Preti, Bolton et al. 2016). Still, under the *Connectomics* framework, even dynamic studies measure spatial

connectivity patterns over time, rather than investigating deeper origins of the signals. These new insights may help resolve the conflicting - yet not mutually exclusive - hypotheses that have been put forth on the nature of functional connectivity, ranging from stochastic resonance(Deco, Jirsa et al. 2009), metastable synchronization (Cabral, Hugues et al. 2011, Ponce-Alvarez, Deco et al. 2015, Cabral, Castaldo et al. 2022), superposition of harmonic modes (Atasoy, Donnelly et al. 2016, Robinson, Zhao et al. 2016, Henderson, Aquino et al. 2022) or transitions between phase-locking patterns (Vohryzek, Deco et al. 2020), among others.

In conclusion, this work reveals evidence for macroscopic oscillatory modes in spontaneous fMRI signals that organize across the brain in standing wave patterns, providing fresh insight into the organizing principles giving rise to intrinsic connectivity networks. Future work disentangling the different underlying sources of the fMRI signal, as well as studying the impact of specific therapeutic effects, such as direct electromagnetic stimulation or pharmacological manipulations, should deepen our understanding of intrinsic oscillatory modes in the brain. Ultimately, by promoting a better understanding of brain dynamics, this work provides new perspectives for the advance in the diagnosis and treatment of brain disorders.

Methods

Experimental Design

All animal experiments followed the European Directive 2010/63 and were preapproved by the Institution's Review Board and the national competent authority.

Ultrafast resting-state fMRI recordings were obtained from a single brain slice of 6 rats scanned under 3 different conditions, namely medetomidine(Weber, Ramos-Cabrer et al. 2006) combined with 3 concentrations of isoflurane: 0% (sedation), 1% (light anaesthesia) and 3% (deep anaesthesia). Two additional postmortem scans were recorded from a seventh rat to serve as baseline. Moreover, resting-state fMRI recordings covering 12 slices of the rat brain were acquired from 3 rats under medetomidine. Below, we elaborate on each phase.

Animal preparation

Long-Evans female rats (*N*=7) weighing 206 ± 16 g and aged 8.3 ± 1.3 weeks were used in this study. Animals were reared in a temperature-controlled room and held under a 12h/12h light/dark cycle with *ad libitum* access to food and water.

Anaesthesia was induced with 5% isoflurane (Vetflurane™, Virbac, France) mixed with oxygen-enriched (27-30%) air in a custom-built plastic box. Rats were then weighed, moved to the animal bed (Bruker, Germany) and isoflurane was reduced to 2.5%. Eye ointment (Bepanthen Eye Drops, Bepanthen, Germany) was applied to prevent eye dryness. A 0.05 mg/kg bolus of medetomidine solution (Dormilan, Vetpharma Animal Health, Spain: 1 mg/ml, diluted 1:10 in saline) was injected subcutaneously 5-8 min after induction, immediately followed by a constant infusion of 0.1 mg/kg/h s.c. of the same solution (*25*), delivered via a syringe pump (GenieTouch™, Kent Scientific, USA) until the end of the experiment, and by a 10 min-long period where isoflurane was gradually decreased to 0%.

fMRI acquisitions began once the animals stabilized in this condition (the time after isoflurane is reported in Table S1

for each scan). For each rat, 2 fMRI scans were first acquired under medetomidine only (sedation condition). Subsequently, fMRI scans were acquired after increasing isoflurane concentration to 1% (light anaesthesia condition) and finally to 3% (deep anaesthesia condition), waiting 10 min after each isoflurane increase for anaesthesia stabilization.

The breathing frequency and rectal temperature were monitored throughout the MRI sessions using a pillow sensor and an optic fiber probe (SA Instruments Inc., Stony Brook, USA), respectively. In the end of the experiments, medetomidine sedation was reverted by injecting 0.25 mg/kg s.c. of atipamezole (Antisedan, Vetpharma Animal Health, Spain: 5 mg/ml, diluted 1:10 in saline).

A seventh rat, reared in the same conditions, was injected with 1 mL (60 mg) pentobarbital i.p. and scanned postmortem with the same MRI protocol to serve as a control.

MRI protocol

Animals were imaged using a 9.4 T BioSpec® MRI scanner (Bruker, Germany) equipped with an AVANCE™ III HD console, producing isotropic pulsed field gradients of up to 660 mT/m with a 120 µs rise time. RF transmission was achieved using an 86 mm-ID quadrature resonator, while a 4-element array cryoprobe (Bruker, Fallanden, Switzerland) was used for signal reception. Following localizer experiments and routine adjustments for center frequency, RF calibration, acquisition of B_0 maps and automatic shimming, anatomical images were acquired using a T_2-weighted RARE sequence in the coronal plane: TR/TE = 2000/36 ms, FOV = 18 x 16.1 mm^2, in-plane resolution = 150 x 150 μm^2, RARE factor = 8, slice thickness = 0.6 mm, 22 slices, t_{acq} = 3 min 28 s, and sagittal plane: TR/TE = 2000/36 ms, FOV = 24 x 16.1 mm^2, in-plane resolution = 150 x 150 μm^2, RARE factor = 8, slice thickness = 0.5 mm, 20 slices, t_{acq} = 3 min 28 s. These images were used to place the slices of interest.

Single-slice ultrafast fMRI acquisitions

To minimize the repetition time, we focused our analysis in a single 1.2 mm-thick slice of the rat brain, choosing a frontal slice that covered a large cortical area and with a FOV of 21 x 21 mm^2, as shown in Fig. S1 A-B. The slice was placed between -0.2 and 1.0 mm from Bregma according to the Paxinos & Watson rat brain atlas(Paxinos and Watson 2009) (Supplementary Figure S1c).

Six resting-state scans (2 per condition) were acquired from each of *N*=6 living rats (totaling 36 scans) using a gradient-echo echo planar imaging (GE-EPI) sequence (TR/TE = 38/11 ms, flip angle = 15°, matrix size = 84 x 84, in-plane resolution = 250 x 250 μm^2, number of time frames = 16000, t_{acq} = 10 min 8 s). Two postmortem scans were acquired with the same parameters. Additionally, a Multi-Gradient Echo sequence (MGE, TE = 2.5:5:97.5 ms, TR = 300 ms, flip angle = 40°, matrix size = 210 x 210, in-plane resolution = 100 x 100 μm^2, t_{acq} = 4 min 12 s) and a Time-Of-Flight (TOF) FLASH sequence (TR/TE = 8.2/3.3 ms, flip angle = 80°, matrix size = 210 x 210, in-plane resolution = 100 x 100 μm^2, t_{acq} = 17 s 219 ms) sequence were acquired from all rats to obtain additional anatomical and vascular information about the slice, respectively. Details of time after isoflurane induction, breathing frequency and rectal temperature are reported for each scan in Table S1.

Whole-brain fMRI acquisitions

Resting-state data was acquired twice under medetomidine sedation from *N*=3 rats using a multi-slice GE-EPI sequence covering the entire rat brain, from the frontal part of the cerebellum to the posterior part of the olfactory bulb, and with the following parameters: TR/TE = 350/11 ms, flip angle = 40°, FOV = 24 x 24 mm^2, matrix size = 70 x 70, in-plane resolution = 342.9 x 342.9 μm^2, slice thickness = 1.2 mm, slice gap = 0.15 mm, 12 slices, number of time frames = 2572, t_{acq} = 15 min 0 s 200 ms.

Brain masks

Individual brain masks were defined manually and aligned across rats to a common central coordinate. All individual rat masks were superposed to define a common brain mask containing *N*=1463 voxels in the single slice and N=7426 voxels in the whole brain.

In the single slice, no spatial or temporal interpolation was applied to the signals, such that the signal in each brain voxel corresponds to the raw fMRI signal recorded.

In multi-slice acquisitions, slice-timing correction was applied using linear interpolation over time.

Space-frequency analysis of fMRI data

Power spectra were computed for the fMRI signals on each of the 84 x 84 = 7056 voxels using the fast Fourier transform, after removing the first 500 frames (19 seconds) and detrending. Voxel power spectra were obtained up to the Nyquist frequency of $(2TR)^{-1}$ = 13.1579 Hz. Images of the power across a selected range of frequencies were obtained by averaging the band-limited power in each voxel across scans in the same condition. All spectral analyses were performed at the single scan level and metrics statistically compared between conditions. Analysis up to the Nyquist frequency are reported in Supplementary Figure S5.

Principal Component analysis

For each scan, the fMRI signals in $N = 1463$ brain voxels were band-pass filtered between 0.01 and 0.3Hz and the NxN covariance matrix was computed. The largest magnitude eigenvalue, λ_1^{PM} was calculated for the two postmortem scans, and the largest one selected as the baseline threshold. The covariance matrices were averaged across the 12 scans in each condition, and, for each condition the α $Nx1$ eigenvectors with eigenvalue $\lambda_\alpha^{condition} > \lambda_1^{PM}$ were extracted, representing the principal components detected in each condition with magnitude above the postmortem baseline.

The same analysis performed using decreasing sampling rates is reported in Supplementary Figures S10. The modes detected using correlation - instead of covariance - above postmortem baseline are reported in Supplementary Figure S11.

Statistical analysis

We compared the power between conditions at different frequency bands using a non-parametric permutation-based t-test (10 000 permutations to ensure robustness of results) to detect the frequency range most sensitive to the 3 different conditions. P-values were conservatively corrected by the number of comparisons performed (Bonferroni correction), considering both the number of between-group comparisons (considering only independent hypotheses) as well as the number of frequency bands considered (considering dependent hypotheses as well, which is even more conservative).

The resonance Q-factors and peak frequencies were statistically compared using the same permutation test.

Standard error is calculated as the standard deviation divided by the square root of the number of values compared.

Resonance analysis

Resonance was evaluated by computing the Q-factor, a measure typically used in acoustics and engineering to quantify resonance phenomena. Importantly, it is not implied by definition that a covariance mode will oscillate, since signals can co-vary aperiodically, without necessarily oscillating. The Q-factors were estimated for the temporal signatures associated to the principal component detected in each condition, for all the 12 scans in each condition and statistically compared between conditions (p-values reported in Table S2).

Damped Oscillator Model

To illustrate the response of an oscillatory system with different damping coefficients, we used the Stuart-Landau equation:

$$\frac{dZ}{dt} = Z\left(i\omega - \left|Z^2\right| + a\right)$$

where Z is complex (with real and imaginary components), ω is the natural frequency, and a defines the position of the system with respect to the Hopf bifurcation at $a = 0$, such that for $a > 0$ the system displays self-sustained oscillations with constant amplitude scaled by a, whereas for $a < 0$ the oscillations are damped and the system decays back to the fixed point equilibrium at $Z = 0$ at a rate scaled by the magnitude of a (i.e., the more negative the a, the stronger the damping).

A single unit pulse (i.e., a Dirac delta function) is applied at t=0 to illustrate the intrinsic response of the system in Supplementary Figure S16. Further, to illustrate the response to continuous perturbation with a stochastic input, we add complex Gaussian white noise as:

$$\frac{dZ}{dt} = Z\left(i\omega - \left|Z^2\right| + a\right) + \beta\eta_1 + i\beta\eta_2,$$

where η_1 and η_2 are independently drawn from a Gaussian distribution with standard deviation $\beta = 1$ (integrated as $\beta\sqrt{dt}$). Simulations were obtained using the Euler method for numerical integration with a time step dt = 10^{-3} seconds.

Acknowledgments

Portuguese Foundation for Science and Technology (FCT) grant UIDB/50026/2020 (JC)
Portuguese Foundation for Science and Technology (FCT) grant UIDP/50026/2020 (JC)
Portuguese Foundation for Science and Technology (FCT) grant CEECIND/03325/2017 (JC)
European Research Council (ERC) grant 679058 (NS, FFF)
Portuguese Foundation for Science and Technology (FCT) grant 275-FCT-PTDC/BBB/IMG/5132/2014 (NS, FFF)
Lisboa Regional Operational Programme (Lisboa 2020), under the PORTUGAL 2020 Partnership Agreement through the European Regional Development Fund (ERDF)
Portuguese Foundation for Science and Technology (FCT) grant LISBOA-01-0145-FEDER-022170.

Author contributions

Conceptualization: JC, NS

Methodology: JC, NS, FFF

Investigation: JC, FFF, NS

Visualization: JC

Funding acquisition: JC, NS

Project administration: NS

Supervision: JC, NS

Writing – original draft: JC, NS

Writing – review & editing: JC, NS, FFF

Competing interests:

Authors declare that they have no competing interests.

Data availability:

All structural and functional MRI data used in this study is available in Maltab format (.mat) in:

https://drive.google.com/drive/u/5/folders/1JQ_1AmP4v-HEB_ll5ZwHEaB0RtIoA17R

which will be deposited in a public database upon acceptance.

Code availability:

All Matlab scripts used for the analysis and figures in this work are made available as supplementary material with this work.

References

Allen, E. A., E. Damaraju, S. M. Plis, E. B. Erhardt, T. Eichele and V. D. Calhoun (2014). "Tracking whole-brain connectivity dynamics in the resting state." Cereb Cortex **24**(3): 663-676.

Arbabi, A., L. S. Noakes, D. Vousden, J. Dazai, S. Spring, O. Botelho, T. Keshavarzian, M. Mattingly, J. Ellegood and L. Nutter (2022). "Multiple-mouse magnetic resonance imaging with cryogenic radiofrequency probes for evaluation of brain development." NeuroImage **252**: 119008.

Ashwin, P., S. Coombes and R. Nicks (2016). "Mathematical frameworks for oscillatory network dynamics in neuroscience." The Journal of Mathematical Neuroscience **6**(1): 1-92.

Atasoy, S., I. Donnelly and J. Pearson (2016). "Human brain networks function in connectome-specific harmonic waves." Nat Commun **7**: 10340.

Belloy, M. E., D. Shah, A. Abbas, A. Kashyap, S. Roßner, A. Van der Linden, S. D. Keilholz, G. A. Keliris and M. Verhoye (2018). "Quasi-periodic patterns of neural activity improve classification of Alzheimer's disease in mice." Scientific reports **8**(1): 1-15.

Biswal, B. B., M. Mennes, X. N. Zuo, S. Gohel, C. Kelly, S. M. Smith, C. F. Beckmann, J. S. Adelstein, R. L. Buckner, S. Colcombe, A. M. Dogonowski, M. Ernst, D. Fair, M. Hampson, M. J. Hoptman, J. S. Hyde, V. J. Kiviniemi, R. Kotter, S. J. Li, C. P. Lin, M. J. Lowe, C. Mackay, D. J. Madden, K. H. Madsen, D. S. Margulies, H. S. Mayberg, K. McMahon, C. S. Monk, S. H. Mostofsky, B. J. Nagel, J. J. Pekar, S. J. Peltier, S. E. Petersen, V. Riedl, S. A. Rombouts, B. Rypma, B. L. Schlaggar, S. Schmidt, R. D. Seidler, G. J. Siegle, C. Sorg, G. J. Teng, J. Veijola, A. Villringer, M. Walter, L. Wang, X. C. Weng, S. Whitfield-Gabrieli, P. Williamson, C. Windischberger, Y. F. Zang, H. Y. Zhang, F. X. Castellanos and M. P. Milham (2010). "Toward discovery science of human brain function." Proc Natl Acad Sci U S A **107**(10): 4734-4739.

Bolt, T., J. S. Nomi, D. Bzdok, J. A. Salas, C. Chang, B. Thomas Yeo, L. Q. Uddin and S. D. Keilholz (2022). "A parsimonious description of global functional brain organization in three spatiotemporal patterns." Nature Neuroscience **25**(8): 1093-1103.

Breakspear, M. (2017). "Dynamic models of large-scale brain activity." Nat Neurosci **20**(3): 340-352.

Bukhari, Q., A. Schroeter, D. M. Cole and M. Rudin (2017). "Resting state fMRI in mice reveals anesthesia specific signatures of brain functional networks and their interactions." Frontiers in neural circuits **11**: 5.

Buzsáki, G. (2006). Rhythms of the brain. Oxford, Oxford University Press,**:** 1 online resource (xiv, 448 p.) ill.

Cabral, J., F. Castaldo, J. Vohryzek, V. Litvak, C. Bick, R. Lambiotte, K. Friston, M. L. Kringelbach and G. Deco (2022). "Metastable oscillatory modes emerge from synchronization in the brain spacetime connectome." Communications Physics **5**(1): 1-13.

Cabral, J., E. Hugues, O. Sporns and G. Deco (2011). "Role of local network oscillations in resting-state functional connectivity." Neuroimage **57**(1): 130-139.

Cabral, J., M. Kringelbach and G. Deco (2017). "Functional Connectivity dynamically evolves on multiple time-scales over a static Structural Connectome: Models and Mechanisms." Neuroimage **160**: 84-96.

Cabral, J., M. L. Kringelbach and G. Deco (2017). "Functional connectivity dynamically evolves on multiple time-scales over a static structural connectome: Models and mechanisms." Neuroimage.

Cabral, J., D. Vidaurre, P. Marques, R. Magalhaes, P. Silva Moreira, J. Miguel Soares, G. Deco, N. Sousa and M. L. Kringelbach (2017). "Cognitive performance in healthy older adults relates to spontaneous switching between states of functional connectivity during rest." Sci Rep **7**(1): 5135.

Calhoun, V. D., R. Miller, G. Pearlson and T. Adali (2014). "The chronnectome: time-varying connectivity networks as the next frontier in fMRI data discovery." Neuron **84**(2): 262-274.

Casorso, J., X. Kong, W. Chi, D. Van De Ville, B. T. Yeo and R. Liégeois (2019). "Dynamic mode decomposition of resting-state and task fMRI." NeuroImage **194**: 42-54.

Chen, J. E. and G. H. Glover (2015). "BOLD fractional contribution to resting-state functional connectivity above 0.1 Hz." Neuroimage **107**: 207-218.

Coletta, L., M. Pagani, J. D. Whitesell, J. A. Harris, B. Bernhardt and A. Gozzi (2020). "Network structure of the mouse brain connectome with voxel resolution." Science Advances **6**(51): eabb7187.

Damoiseaux, J. S., S. A. Rombouts, F. Barkhof, P. Scheltens, C. J. Stam, S. M. Smith and C. F. Beckmann (2006). "Consistent resting-state networks across healthy subjects." Proc Natl Acad Sci U S A **103**(37): 13848-13853.

Deco, G., J. Cabral, M. W. Woolrich, A. B. Stevner, T. J. van Hartevelt and M. L. Kringelbach (2017). "Single or multiple frequency generators in on-going brain activity: A mechanistic whole-brain model of empirical MEG data." Neuroimage **152**: 538-550.

Deco, G., J. Cruzat, J. Cabral, E. Tagliazucchi, H. Laufs, N. K. Logothetis and M. L. Kringelbach (2019). "Awakening: Predicting external stimulation to force transitions between different brain states." Proceedings of the National Academy of Sciences **116**(36): 18088-18097.

Deco, G., V. Jirsa, A. R. McIntosh, O. Sporns and R. Kotter (2009). "Key role of coupling, delay, and noise in resting brain fluctuations." Proc Natl Acad Sci U S A **106**(25): 10302-10307.

Deco, G., V. K. Jirsa, P. A. Robinson, M. Breakspear and K. Friston (2008). "The dynamic brain: from spiking neurons to neural masses and cortical fields." PLoS Comput Biol **4**(8): e1000092.

Drew, P. J., C. Mateo, K. L. Turner, X. Yu and D. Kleinfeld (2020). "Ultra-slow oscillations in fMRI and resting-state connectivity: neuronal and vascular contributions and technical confounds." Neuron **107**(5): 782-804.

Eickhoff, S. B., D. Bzdok, A. R. Laird, C. Roski, S. Caspers, K. Zilles and P. T. Fox (2011). "Co-activation patterns distinguish cortical modules, their connectivity and functional differentiation." Neuroimage **57**(3): 938-949.

Engel, A. K., P. Fries and W. Singer (2001). "Dynamic predictions: oscillations and synchrony in top-down processing." Nat Rev Neurosci **2**(10): 704-716.

Fornito, A., A. Zalesky and M. Breakspear (2015). "The connectomics of brain disorders." Nat Rev Neurosci **16**(3): 159-172.

Fox, M. D. and M. E. Raichle (2007). "Spontaneous fluctuations in brain activity observed with functional magnetic resonance imaging." Nature reviews neuroscience **8**(9): 700-711.

Friston, K. J., J. Kahan, A. Razi, K. E. Stephan and O. Sporns (2014). "On nodes and modes in resting state fMRI." NeuroImage **99**: 533-547.

Fulcher, B. D., J. D. Murray, V. Zerbi and X.-J. Wang (2019). "Multimodal gradients across mouse cortex." Proceedings of the National Academy of Sciences **116**(10): 4689-4695.

Fultz, N. E., G. Bonmassar, K. Setsompop, R. A. Stickgold, B. R. Rosen, J. R. Polimeni and L. D. Lewis (2019). "Coupled electrophysiological, hemodynamic, and cerebrospinal fluid oscillations in human sleep." Science **366**(6465): 628-631.

Gabay, N. C., T. Babaie-Janvier and P. A. Robinson (2018). "Dynamics of cortical activity eigenmodes including standing, traveling, and rotating waves." Physical Review E **98**(4): 042413.

Gabay, N. C. and P. Robinson (2017). "Cortical geometry as a determinant of brain activity eigenmodes: Neural field analysis." Physical Review E **96**(3): 032413.

Gil, R., F. F. Fernandes and N. Shemesh (2021). "Neuroplasticity-driven timing modulations revealed by ultrafast functional magnetic resonance imaging." Neuroimage **225**: 117446.

Gonzalez-Castillo, J., Z. S. Saad, D. A. Handwerker, S. J. Inati, N. Brenowitz and P. A. Bandettini (2012). "Whole-brain, time-locked activation with simple tasks revealed using massive averaging and model-free analysis." Proc Natl Acad Sci U S A **109**(14): 5487-5492.

Gozzi, A. and V. Zerbi (2022). "Modelling brain dysconnectivity in rodents." Biological Psychiatry.

Grandjean, J., A. Schroeter, I. Batata and M. Rudin (2014). "Optimization of anesthesia protocol for resting-state fMRI in mice based on differential effects of anesthetics on functional connectivity patterns." Neuroimage **102**: 838-847.

Gu, Y., L. E. Sainburg, S. Kuang, F. Han, J. W. Williams, Y. Liu, N. Zhang, X. Zhang, D. A. Leopold and X. Liu (2021). "Brain activity fluctuations propagate as waves traversing the cortical hierarchy." Cerebral cortex **31**(9): 3986-4005.

Gutierrez-Barragan, D., M. A. Basson, S. Panzeri and A. Gozzi (2019). "Infraslow state fluctuations govern spontaneous fMRI network dynamics." Current Biology **29**(14): 2295-2306. e2295.

Gutierrez-Barragan, D., N. A. Singh, F. G. Alvino, L. Coletta, F. Rocchi, E. De Guzman, A. Galbusera, M. Uboldi, S. Panzeri and A. Gozzi (2022). "Unique spatiotemporal fMRI dynamics in the awake mouse brain." Current Biology **32**(3): 631-644. e636.

Hansen, E. C., D. Battaglia, A. Spiegler, G. Deco and V. K. Jirsa (2015). "Functional connectivity dynamics: modeling the switching behavior of the resting state." Neuroimage **105**: 525-535.

He, B. J., A. Z. Snyder, J. M. Zempel, M. D. Smyth and M. E. Raichle (2008). "Electrophysiological correlates of the brain's intrinsic large-scale functional architecture." Proc Natl Acad Sci U S A **105**(41): 16039-16044.

Henderson, J. A., K. M. Aquino and P. Robinson (2022). "Empirical estimation of the eigenmodes of macroscale cortical dynamics: Reconciling neural field eigenmodes and resting-state networks." Neuroimage: Reports **2**(3): 100103.

Huntenburg, J. M., P.-L. Bazin and D. S. Margulies (2018). "Large-scale gradients in human cortical organization." Trends in cognitive sciences **22**(1): 21-31.

Hutchison, R. M., L. S. Leung, S. M. Mirsattari, J. S. Gati, R. S. Menon and S. Everling (2011). "Resting-state networks in the macaque at 7 T." Neuroimage **56**(3): 1546-1555.

Hutchison, R. M., T. Womelsdorf, E. A. Allen, P. A. Bandettini, V. D. Calhoun, M. Corbetta, S. Della Penna, J. H. Duyn, G. H. Glover, J. Gonzalez-Castillo, D. A. Handwerker, S. Keilholz, V. Kiviniemi, D. A. Leopold, F. de Pasquale, O. Sporns, M. Walter and C. Chang (2013). "Dynamic functional connectivity: promise, issues, and interpretations." Neuroimage **80**: 360-378.

Jirsa, V. K. and H. Haken (1996). "Field theory of electromagnetic brain activity." Physical review letters **77**(5): 960.

Kay, K., K. W. Jamison, R.-Y. Zhang and K. Uğurbil (2020). "A temporal decomposition method for identifying venous effects in task-based fMRI." Nature methods **17**(10): 1033-1039.

Lake, E. M., X. Ge, X. Shen, P. Herman, F. Hyder, J. A. Cardin, M. J. Higley, D. Scheinost, X. Papademetris and M. C. Crair (2020). "Simultaneous cortex-wide fluorescence Ca2+ imaging and whole-brain fMRI." Nature methods **17**(12): 1262-1271.

Lee, H.-L., B. Zahneisen, T. Hugger, P. LeVan and J. Hennig (2013). "Tracking dynamic resting-state networks at higher frequencies using MR-encephalography." Neuroimage **65**: 216-222.

Lewis, L. D., K. Setsompop, B. R. Rosen and J. R. Polimeni (2016). "Fast fMRI can detect oscillatory neural activity in humans." Proceedings of the national academy of sciences **113**(43): E6679-E6685.

Liu, X. and J. H. Duyn (2013). "Time-varying functional network information extracted from brief instances of spontaneous brain activity." Proc Natl Acad Sci U S A **110**(11): 4392-4397.

Liu, X., N. Zhang, C. Chang and J. H. Duyn (2018). "Co-activation patterns in resting-state fMRI signals." Neuroimage **180**: 485-494.

Lord, L.-D., P. Expert, S. Atasoy, L. Roseman, K. Rapuano, R. Lambiotte, D. J. Nutt, G. Deco, R. L. Carhart-Harris and M. L. Kringelbach (2019). "Dynamical exploration of the repertoire of brain networks at rest is modulated by psilocybin." NeuroImage **199**: 127-142.

Lu, H., Q. Zou, H. Gu, M. E. Raichle, E. A. Stein and Y. Yang (2012). "Rat brains also have a default mode network." Proceedings of the National Academy of Sciences **109**(10): 3979-3984.

Margulies, D. S., S. S. Ghosh, A. Goulas, M. Falkiewicz, J. M. Huntenburg, G. Langs, G. Bezgin, S. B. Eickhoff, F. X. Castellanos and M. Petrides (2016). "Situating the default-mode network along a principal gradient of macroscale cortical organization." Proceedings of the National Academy of Sciences **113**(44): 12574-12579.

Mateo, C., P. M. Knutsen, P. S. Tsai, A. Y. Shih and D. Kleinfeld (2017). "Entrainment of arteriole vasomotor fluctuations by neural activity is a basis of blood-oxygenation-level-dependent "resting-state" connectivity." Neuron **96**(4): 936-948. e933.

Mukta, K., J. MacLaurin and P. Robinson (2017). "Theory of corticothalamic brain activity in a spherical geometry: Spectra, coherence, and correlation." Physical Review E **96**(5): 052410.

Nasrallah, F. A., H.-C. Tay and K.-H. Chuang (2014). "Detection of functional connectivity in the resting mouse brain." Neuroimage **86**: 417-424.

Nunez, P. L. (1974). "The brain wave equation: a model for the EEG." Mathematical Biosciences **21**(3-4): 279-297.

Nunez, P. L. and R. Srinivasan (2014). "Neocortical dynamics due to axon propagation delays in cortico-cortical fibers: EEG traveling and standing waves with implications for top-down influences on local networks and white matter disease." Brain Res **1542**: 138-166.

Paasonen, J., P. Stenroos, R. A. Salo, V. Kiviniemi and O. Gröhn (2018). "Functional connectivity under six anesthesia protocols and the awake condition in rat brain." Neuroimage **172**: 9-20.

Pan, W.-J., G. J. Thompson, M. E. Magnuson, D. Jaeger and S. Keilholz (2013). "Infraslow LFP correlates to resting-state fMRI BOLD signals." Neuroimage **74**: 288-297.

Paxinos, G. and C. Watson (2009). The Rat Brain in Stereotaxic Coordinates, Elsevier/Academic.

Ponce-Alvarez, A., G. Deco, P. Hagmann, G. L. Romani, D. Mantini and M. Corbetta (2015). "Resting-state temporal synchronization networks emerge from connectivity topology and heterogeneity." PLoS Comput Biol **11**(2): e1004100.

Pradier, B., L. Wachsmuth, N. Nagelmann, D. Segelcke, S. Kreitz, A. Hess, E. M. Pogatzki-Zahn and C. Faber (2021). "Combined resting state-fMRI and calcium recordings show stable brain states for task-induced fMRI in mice under combined ISO/MED anesthesia." NeuroImage **245**: 118626.

Preti, M. G., T. A. Bolton and D. Van De Ville (2016). "The dynamic functional connectome: State-of-the-art and perspectives." Neuroimage.

Preti, M. G., T. A. Bolton and D. Van De Ville (2017). "The dynamic functional connectome: State-of-the-art and perspectives." Neuroimage **160**: 41-54.

Ratering, D., C. Baltes, J. Nordmeyer-Massner, D. Marek and M. Rudin (2008). "Performance of a 200-MHz cryogenic RF probe designed for MRI and MRS of the murine brain." Magnetic Resonance in Medicine: An Official Journal of the International Society for Magnetic Resonance in Medicine **59**(6): 1440-1447.

Raut, R. V., A. Z. Snyder, A. Mitra, D. Yellin, N. Fujii, R. Malach and M. E. Raichle (2021). "Global waves synchronize the brain's functional systems with fluctuating arousal." Science advances **7**(30): eabf2709.

Robinson, P. A., J. A. Henderson, N. C. Gabay, K. M. Aquino, T. Babaie-Janvier and X. Gao (2021). "Determination of dynamic brain connectivity via spectral analysis." Frontiers in Human Neuroscience: 360.

Robinson, P. A., C. J. Rennie and J. J. Wright (1997). "Propagation and stability of waves of electrical activity in the cerebral cortex." Physical Review E **56**(1): 826.

Robinson, P. A., X. Zhao, K. M. Aquino, J. D. Griffiths, S. Sarkar and G. Mehta-Pandejee (2016). "Eigenmodes of brain activity: Neural field theory predictions and comparison with experiment." Neuroimage **142**: 79-98.

Rocchi, F., C. Canella, S. Noei, D. Gutierrez-Barragan, L. Coletta, A. Galbusera, A. Stuefer, S. Vassanelli, M. Pasqualetti and G. Iurilli (2022). "Increased fMRI connectivity upon chemogenetic inhibition of the mouse prefrontal cortex." Nature communications **13**(1): 1-15.

Sapoval, B., T. Gobron and A. Margolina (1991). "Vibrations of fractal drums." Physical review letters **67**(21): 2974.

Schmid, P. J. (2010). "Dynamic mode decomposition of numerical and experimental data." Journal of fluid mechanics **656**: 5-28.

Schwalm, M., F. Schmid, L. Wachsmuth, H. Backhaus, A. Kronfeld, F. A. Jury, P.-H. Prouvot, C. Fois, F. Albers and T. van Alst (2017). "Cortex-wide BOLD fMRI activity reflects locally-recorded slow oscillation-associated calcium waves." Elife **6**: e27602.

Smith, S. M., P. T. Fox, K. L. Miller, D. C. Glahn, P. M. Fox, C. E. Mackay, N. Filippini, K. E. Watkins, R. Toro and A. R. Laird (2009). "Correspondence of the brain's functional architecture during activation and rest." Proceedings of the national academy of sciences **106**(31): 13040-13045.

Stam, C. J. (2014). "Modern network science of neurological disorders." Nat Rev Neurosci **15**(10): 683-695.

Stevner, A. B. A., D. Vidaurre, J. Cabral, K. Rapuano, S. F. V. Nielsen, E. Tagliazucchi, H. Laufs, P. Vuust, G. Deco, M. W. Woolrich, E. Van Someren and M. L. Kringelbach (2019). "Discovery of key whole-brain transitions and dynamics during human wakefulness and non-REM sleep." Nature Communications **10**(1): 1035.

Teschl, G. (2012). Ordinary differential equations and dynamical systems, American Mathematical Soc.

Tewarie, P., R. Abeysuriya, Á. Byrne, G. C. O'Neill, S. N. Sotiropoulos, M. J. Brookes and S. Coombes (2018). "How do spatially distinct frequency specific MEG networks emerge from one underlying structural connectome? The role of the structural eigenmodes." NeuroImage.

Thompson, G. J., W.-J. Pan, M. E. Magnuson, D. Jaeger and S. D. Keilholz (2014). "Quasi-periodic patterns (QPP): large-scale dynamics in resting state fMRI that correlate with local infraslow electrical activity." Neuroimage **84**: 1018-1031.

Toi, P. T., H. J. Jang, K. Min, S.-P. Kim, S.-K. Lee, J. Lee, J. Kwag and J.-Y. Park (2022). "In vivo direct imaging of neuronal activity at high temporospatial resolution." Science **378**(6616): 160-168.

Trapp, C., K. Vakamudi and S. Posse (2018). "On the detection of high frequency correlations in resting state fMRI." Neuroimage **164**: 202-213.

Uddin, L. Q., B. Yeo and R. N. Spreng (2019). "Towards a universal taxonomy of macro-scale functional human brain networks." Brain topography **32**(6): 926-942.

van Alst, T. M., L. Wachsmuth, M. Datunashvili, F. Albers, N. Just, T. Budde and C. Faber (2019). "Anesthesia differentially modulates neuronal and vascular contributions to the BOLD signal." Neuroimage **195**: 89-103.

van den Berg, M., M. H. Adhikari, M. Verschuuren, I. Pintelon, T. Vasilkovska, J. Van Audekerke, S. Missault, L. Heymans, P. Ponsaerts and W. H. De Vos (2022). "Altered basal forebrain function during whole-brain network activity at pre-and early-plaque stages of Alzheimer's disease in TgF344-AD rats." Alzheimer's research & therapy **14**(1): 1-21.

Vohryzek, J., G. Deco, B. Cessac, M. L. Kringelbach and J. Cabral (2020). "Ghost attractors in spontaneous brain activity: Recurrent excursions into functionally-relevant BOLD phase-locking states." Frontiers in systems neuroscience **14**: 20.

Wang, X. J. (2010). "Neurophysiological and computational principles of cortical rhythms in cognition." Physiol Rev **90**(3): 1195-1268.

Weber, R., P. Ramos-Cabrer, D. Wiedermann, N. Van Camp and M. Hoehn (2006). "A fully noninvasive and robust experimental protocol for longitudinal fMRI studies in the rat." Neuroimage **29**(4): 1303-1310.

Wu, T. L., A. Mishra, F. Wang, P. F. Yang, J. C. Gore and L. M. Chen (2016). "Effects of isoflurane anesthesia on resting-state fMRI signals and functional connectivity within primary somatosensory cortex of monkeys." Brain and behavior **6**(12): e00591.

Xie, X., C. Cai, P. F. Damasceno, S. S. Nagarajan and A. Raj (2021). "Emergence of canonical functional networks from the structural connectome." NeuroImage **237**: 118190.

Yousefi, B., J. Shin, E. H. Schumacher and S. D. Keilholz (2018). "Quasi-periodic patterns of intrinsic brain activity in individuals and their relationship to global signal." Neuroimage **167**: 297-308.

Yu, X., Y. He, M. Wang, H. Merkle, S. J. Dodd, A. C. Silva and A. P. Koretsky (2016). "Sensory and optogenetically driven single-vessel fMRI." Nature methods **13**(4): 337-340.

Yu, X., C. Qian, D.-y. Chen, S. J. Dodd and A. P. Koretsky (2014). "Deciphering laminar-specific neural inputs with line-scanning fMRI." Nature methods **11**(1): 55-58.

Zerbi, V., A. Floriou-Servou, M. Markicevic, Y. Vermeiren, O. Sturman, M. Privitera, L. von Ziegler, K. D. Ferrari, B. Weber and P. P. De Deyn (2019). "Rapid reconfiguration of the functional connectome after chemogenetic locus coeruleus activation." Neuron **103**(4): 702-718. e705.